ornl

ORNL/GWPO-025

OAK RIDGE NATIONAL LABORATORY

LOCKHEED MARTIN

Effective Porosity and Pore-Throat Sizes of Mudrock Saprolite from the Nolichucky Shale Within Bear Creek Valley on the Oak Ridge Reservation: Implications for Contaminant Transport and Retardation Through Matrix Diffusion

J. Dorsch
T. J. Katsube

MANAGED AND OPERATED BY
LOCKHEED MARTIN ENERGY RESEARCH CORPORATION
FOR THE UNITED STATES
DEPARTMENT OF ENERGY

RB

ORNL/GWPO-025

EFFECTIVE POROSITY AND PORE-THROAT SIZES OF MUDROCK SAPROLITE FROM THE NOLICHUCKY SHALE WITHIN BEAR CREEK VALLEY ON THE OAK RIDGE RESERVATION: IMPLICATIONS FOR CONTAMINANT TRANSPORT AND RETARDATION THROUGH MATRIX DIFFUSION

J. Dorsch[1]

T. J. Katsube[2]

[1] Environmental Sciences Division, Oak Ridge National Laboratory, Oak Ridge, TN 37831-6400
[2] Geological Survey of Canada, Mineral Resources Division, Ottawa, Ontario K1A 0E8

Date Issued--May, 1996

Prepared by the
Environmental Sciences Division
Oak Ridge National Laboratory

Prepared for
Groundwater Program Office
under budget and reporting code EU 2010301
OAK RIDGE NATIONAL LABORATORY
Oak Ridge, Tennessee 37831-6285
managed by
LOCKHEED MARTIN ENERGY RESEARCH, CORP.
for the
US DEPARTMENT OF ENERGY
under contract DE-AC05-96OR22464

Table of Contents

FIGURES

TABLES

ACKNOWLEDGMENTS

Gerilynn R. Moline and William E. Sanford are thanked for critically reading a previous draft of this report which resulted in significant improvements. Mark P. Elles is acknowledged for his time discussing aspect of soil and saprolite characteristics in the core barn. Any shortcomings, however, remain the responsibility of the authors. The support from the Y-12 HSE&A-Division, administered through Judy A. Hodgins is most gratefully acknowledged. The research was supported in part by an appointment to the Oak Ridge National Laboratory Postdoctoral Research Associates Program (awarded to J. Dorsch) administered jointly by the Oak Ridge National Laboratory and the Oak Ridge Institute for Science and Education.

EXECUTIVE SUMMARY

Matrix diffusion is regarded as an important transport mechanism within the low-permeability dual-porosity saprolite mantle on the Oak Ridge Reservation (ORR). In order to evaluate and model matrix diffusion, a knowledge of the effective porosity of the saprolite matrix is necessary. To that end, mudrock-saprolite specimens from Bear Creek Valley on the ORR, developed from the Nolichucky Shale through weathering, were analyzed with helium and mercury porosimetry. The saprolite matrix of the fresh core samples is composed of the volumetrically more abundant saprolite groundmass which contains varying fractions of less weathered mudrock-fragments. Average effective porosities determined by helium porosimetry, judged to provide the best estimate for true (maximum) effective porosity, are 16.1% for mudrock fragments and 39.0% for groundmass. Average effective porosities from mercury porosimetry are 11.9% for mudrock fragments and 33.7% (Hg2) or 26.8% (Hg1) for groundmass. The progressive effect of weathering is apparent through an increase in effective porosity combined with a decrease in bulk-density, when specimens of bedrock mudrock, saprolite mudrock-fragments, and saprolite groundmass are compared. Weathering most likely involved the loss of cement and of some grain material, and the mechanical loosening of the grain fabric. Pore-throat-size distribution curves for saprolite mudrock-fragments (skewed right, modes 5 to 20 nm, majority of pore throats <100 nm) are distinctly different from distribution curves of saprolite groundmass (skewed left, modes 1200 to 5000 nm, majority of pore throats >100 nm). Together with the overall shift of the throat-size spectrum toward larger sizes for specimens of bedrock mudrock, saprolite mudrock-fragments, and saprolite groundmass, this again reflects the increasing effect of weathering. The distribution curves also point out that the boundaries of weathering zones are most likely irregular and not parallel to the ground surface. Calculated interval effective porosities characterize larger volumes of saprolite matrix and integrate both mudrock-fragment and groundmass effective porosities. The values range from 51.3% to 26.2% and display a smooth decrease with depth, mirroring the saprolite weathering profile. The calculated interval effective porosities are probably best suited for the task of modeling and evaluating matrix diffusion as a transport mechanism within the saprolite mantle.

PURPOSE

The purpose of the research reported in this document was the derivation of quantitative data on effective porosity and pore-throat sizes of mudrock saprolite based on state-of-the art petrophysical measurement techniques. The target was the saprolite developed from the Nolichucky Shale of the Conasauga Group within Bear Creek Valley on the Oak Ridge Reservation (ORR). The data are important for the evaluation of matrix diffusion as a transport process within fractured low-permeability geological material such as mudrock saprolite on the ORR.

INTRODUCTION

Specimens of saprolite developed from mudrock of the Nolichucky Shale (Upper Cambrian, Conasauga Group) from the Whiteoak Mountain thrust sheet on the Oak Ridge Reservation (ORR) were analyzed. Petrophysical techniques include helium porosimetry and mercury porosimetry. Petrophysical data obtained from the laboratory experiments include effective porosity, pore-throat sizes and their distribution, specimen bulk-density, and specimen grain-density. It is expected that the data from this study will significantly contribute to constraining the modeling of the hydrologic behavior of saprolite developed from mudrock of the Conasauga Group in general and from the Nolichucky Shale specifically.

Conasauga Group Saprolite on the Oak Ridge Reservation

Saprolite is commonly defined (following Fairbridge, 1968, p. 933) as chemically altered, but coherent and not texturally disintegrated rock rotten in situ. Weathering has removed certain chemical components, but the grain relations remain undisturbed. Saprolite occupies the zone below the soil horizons and above the bedrock proper. Lietzke (1992) emphasized especially the leaching of calcium carbonate from Conasauga Group lithologies on the ORR.

The thickness of saprolite on the ORR is highly variable (Lietzke, 1992), but common thicknesses of saprolite developed from the Conasauga Group of up to 10 m are reported (Solomon et al., 1992; Lee et al., 1992). Saprolite retains the structural style obtained by the different clastic lithologies on the ORR (Dreier et al., 1987) predominantly during the Late Paleozoic Alleghanian orogeny. The structural inventory includes different fold generations, faults, and especially a pervasive fracture system. The system is characterized by distinct fracture sets of differing orientation, and was formed during a time span ranging from the Cambrian to the Recent (Lemiszki and Hatcher, 1992).

Four broad hydrologic zones can be identified on the ORR: the near-surface stormflow zone, the vadose zone, the groundwater zone, and the aquiclude (Figure 1; Solomon et al., 1992). Within this hydrologic zonation, mudrock saprolite can be found from the lower part of the stormflow zone, through the vadose zone, down to the water-table interval of the groundwater zone. The degree of weathering generally decreases when moving downward in this section, with a broad transition interval into bedrock. Water saturation occurs within the water-table interval (and below) and (partly to

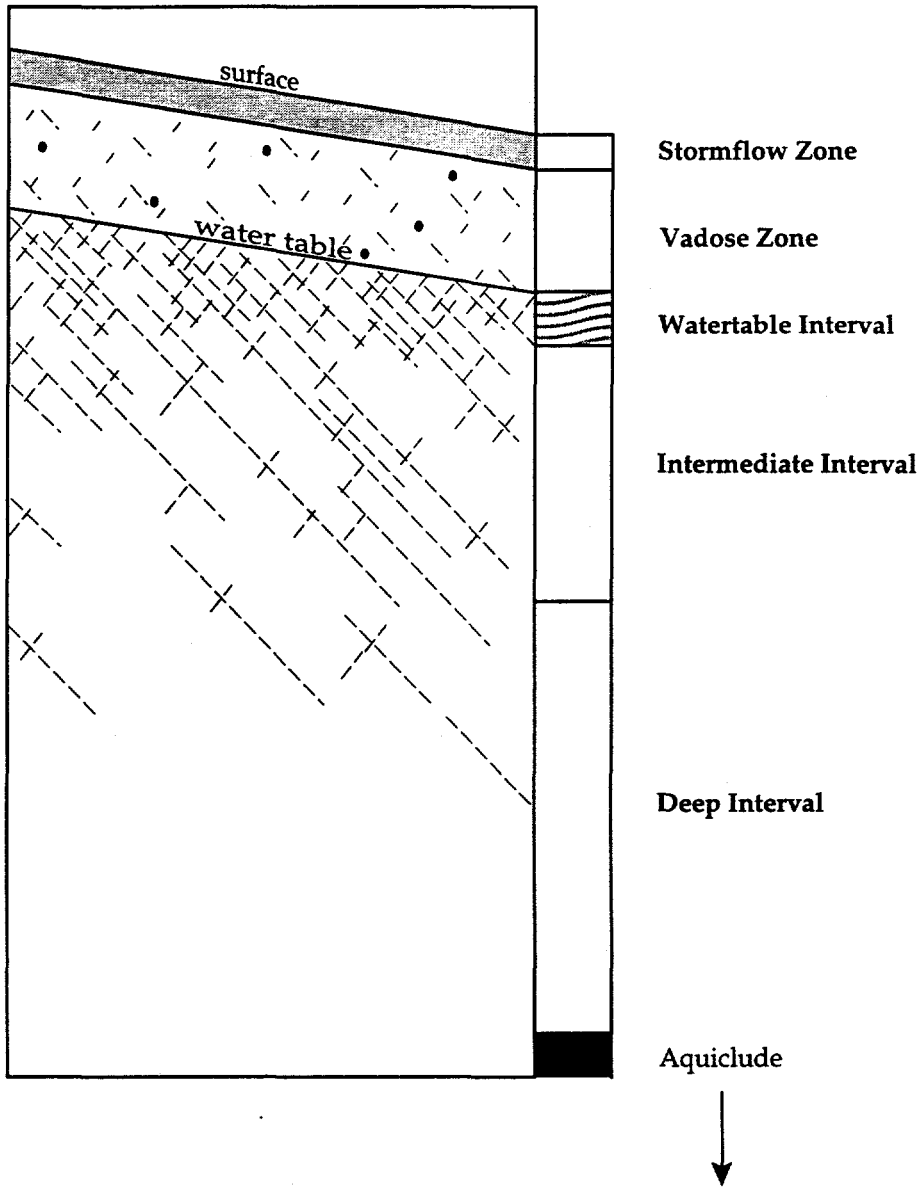

Fig. 1: Schematic vertical relationship of flow zones within aquitards on the ORR (modified after Solomon et al., 1992).

completely) within the stormflow zone during rain events. Seasonal fluctuations are important in extending the water-table interval into what commonly is the vadose zone. The transition zone from regolith (including saprolite) to bedrock typically can be placed at the base of the water-table interval (Solomon et al., 1992).

The Conasauga Group on the ORR is composed predominantly of mudrock, interbedded with limestone beds (Hasson and Haase, 1988, Dreier et al., 1992). The saprolite developed from the Conasauga Group is most important for environmental concerns on the ORR because the Conasauga Group forms an important aquitard unit (Solomon et al., 1992), and a majority of the waste-disposal activities on the ORR are situated within the saprolite interval above Conasauga bedrock. Excavations routinely intersect the water-table interval. Leakage of material from waste-disposal sites has the potential to contaminate the saprolite, which might be further aggravated by transport of contaminant species through the interconnected fracture system.

Saprolite developed from Conasauga Group mudrock is not expected to be uniform in petrophysical characteristics. The petrophysical characteristics are determined by: 1) the original lithologic variance of the deposits, 2) the diagenetic overprint of the deposits and, most importantly, 3) the difference in weathering. Typical soil-saprolite-bedrock weathering profiles (Figure 2) display a change in the severity of weathering with depth which is expected to be reflected by a commensurate change in petrophysical characteristics from the boundary of the soil B-horizon/C-horizon, through the leached (Cr1) and unleached (Cr2) saprolite zones, to the contact with bedrock (Figure 2). A drastic change in petrophysical characteristics from the weathering profile to the unweathered bedrock is also expected (Lietzke et al., 1988). This is a qualitative statement because quantitative data on saprolite petrophysical characteristics are not available at the present. Extensive quantitative petrophysical data, however, are available for mudrock of the Conasauga Group below the saprolite zone (Dorsch et al., 1996). This will provide the opportunity to compare the petrophysical characteristics of bedrock with those of saprolite developed from Conasauga Group mudrock. A general summary of the sedimentology and stratigraphy of the Conasauga Group mudrock (bedrock) is provided by Dorsch et al. (1996).

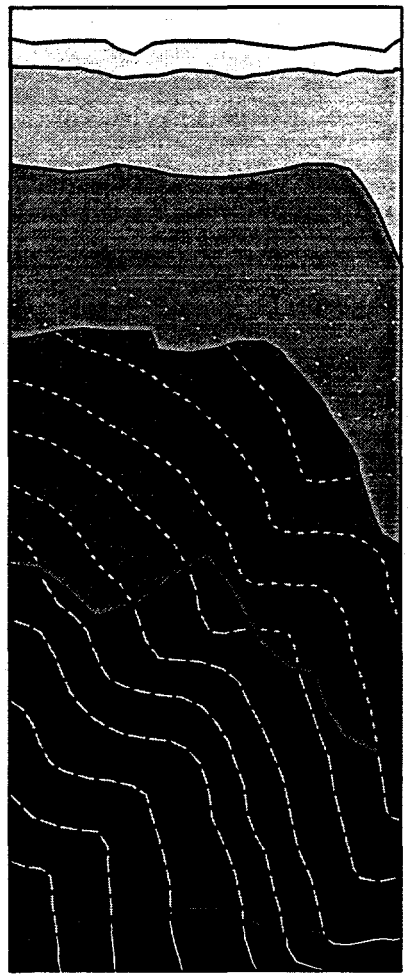

A horizon: *zone of leaching and accumulation of carbon*

E horizon: *zone of intense leaching and loss of clays and oxides*

B horizon: *zone of accumulation of clays and oxides*

C horizon: *zone of lower biologic activity*

Cr horizon: *paralithic material that preclude roots*

Cr1: *oxidized and leached saprolite*

Cr2: *oxidized and unleached saprolite*

R: *lithic material, unoxidized and unleached bedrock*

Fig. 2: Soil-saprolite-bedrock weathering column (modified from Lietzke et al., 1988).

Matrix Diffusion and Effective Porosity

Effective porosity is defined as the ratio of volume of interconnected pore space to total volume of a rock sample. Effective porosity is believed to be an important parameter that controls the extent and effectiveness of diffusive processes within fine-grained siliciclastic rocks (e. g., Germain and Frind, 1989; Toran et al., 1995). The importance of matrix diffusion as an agent for efficient material transport in the fractured low-permeability sedimentary rocks and saprolite on the Oak Ridge Reservation was pointed out by Wickliff et al. (1991), Solomon et al. (1992), Shevenell et al. (1994), and Sanford et al. (1994).

Figure 3 illustrates the potential importance of matrix diffusion for contaminant transport within fractured low-permeability mudrock saprolite. Contaminated water actively moves through the interconnected fracture network, but through the process of diffusion contaminants are able to access the interconnected pore space of the surrounding matrix blocks. Access to the pore water of the saprolite matrix is through matrix pores connected to the fracture network. The result of this mass transfer by diffusion will be an apparent retardation of the spread of the contaminant species carried by water within the interconnected fracture network (e. g., Neretnieks, 1980, Tang et al., 1981; McKay et al., 1993). This scenario will develop while the primary contaminant source is present and active. After removal of the primary contaminant source, either through remediation efforts or through simple depletion, the direction of diffusion will reverse. Contaminants will diffuse out of the matrix into the fracture network now occupied by uncontaminated water. This will lead to the development of a secondary contaminant source, which might be active for a long period and which will be very difficult and expensive to remediate because of the required long time spans for removing the contaminants from the matrix pore-space (e. g., Germain and Frind, 1989; McKay et al., 1993). Accurate knowledge of effective porosity, therefore, is important for modeling and evaluating the possible apparent retardation of contaminant spread and the possible development of secondary contaminant sources within fractured mudrock saprolite (Toran et al., 1995).

The effective porosity of the Conasauga Group mudrock-saprolite matrix can be considered to consist of a sedimentary porosity and of microfractures. The sedimentary porosity developed following deposition and after experiencing compaction, chemical diagenesis (cementation, dissolution), and weathering to saprolite. Microfractures are considered tectonic in origin and are small enough to be part of the saprolite matrix. The

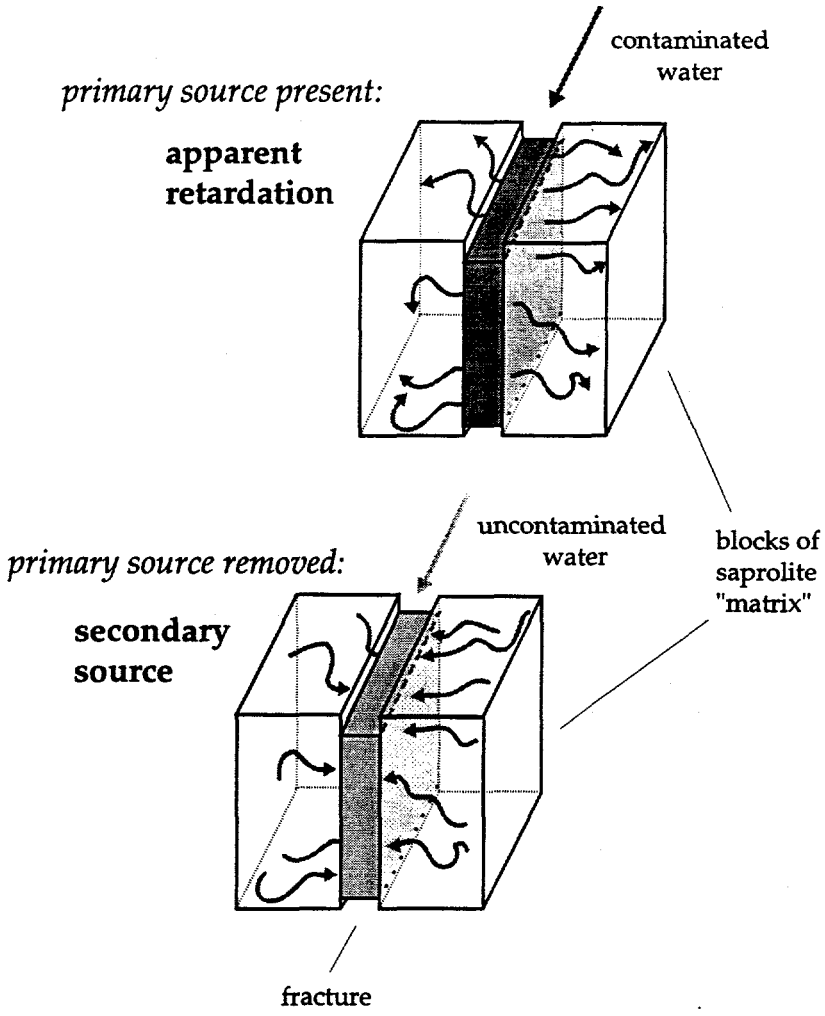

Fig. 3: Schematic block diagrams illustrating the diffusion of contaminant species from a fracture into the surrounding saprolite "matrix" (apparent retardation) and vice versa (secondary contaminant source) (from Dorsch et al., 1996).

tectonic origin of the microfractures remains speculative, however, because detailed petrographic investigations on bedrock mudrock addressing this question are lacking. Larger microfractures, fractures and voids, abundant in the saprolite mantle, cause the saprolite sample to fall apart into smaller integral matrix blocks. These larger openings within the saprolite mantle were not characterized in this study, but they are important for rapid flow and transport through the saprolite zone (Solomon et al., 1992). That these larger openings are preferential flow paths is indicated by Fe-oxides and Mn-oxides coating the walls of the openings, and by translocated clay partially filling the openings (Gwo et al., 1996). The effective porosity data reported in this document are a measure of the space potentially available for diffusive processes within the low-permeability saprolite matrix.

PETROPHYSICAL MEASUREMENT TECHNIQUES

Petrophysical data (effective porosity, specimen grain-density, specimen bulk-density, and pore-throat sizes) for mudrock saprolite were obtained using state-of-the-art laboratory-based measurement techniques. These techniques include helium porosimetry and mercury porosimetry which had been applied previously to fine-grained, low-permeability sedimentary rocks (Issler and Katsube, 1994; Loman et al., 1993; Katsube et al., 1992; Katsube and Scromeda, 1991; Katsube and Best, 1992; Soeder, 1988; Dorsch et al., 1996). Both of these techniques generate petrophysical data using a specimen size of less than 10 g.

The specimens used for the petrophysical measurements were dried at temperatures above 100°C. This was carried out to ensure the determination of all interconnected pore space available for water storage. Drying of specimens above 100°C will drive off all pore water in the specimen and all water adsorbed to clay minerals (Scromeda and Katsube, 1993). The drying procedure will not affect the crystal-lattice water, which is part of the clay minerals (Dorsch, 1995).

Mercury Porosimetry

Principle. Mercury porosimetry involves the forceful injection of a non-wetting liquid (mercury) into a specimen in discrete pressure steps using a mercury porosimeter. The pressures required to force mercury into the specimen correspond to the size of the pore throats and pores (Washburn, 1921; Rootare, 1970; Wardlaw, 1976; Kopaska-Merkel, 1988; Wardlaw et al., 1988; Kopaska-Merkel, 1991). With each increasing pressure step, successively smaller pore throats are accessed by mercury. Mercury porosimetry results are displayed as capillary-pressure curves that plot the amount of intruded mercury versus injection pressure (Figure 4). The amount of intruded mercury can be converted to volume of mercury, and the injection pressure can be converted to pore-throat diameters with the Washburn Equation (see below). Mercury porosimetry, therefore, provides quantitative information on the distribution of pore-throat sizes. The sizes of pore throats are important because they control access to pores. Pores of the same size might be accessed through throats of different sizes, but mercury enters the pore space only after a certain injection pressure is reached (Figure 5). The pore space with the larger sized pore throat will be accessed earlier (at a lower injection pressure) than the pore space of equal size but with a smaller pore throat.

Washburn Equation. The Washburn Equation relates the amount of pressure required to force mercury into pores to the pore-throat diameter greater or equal to d (e. g., Katsube and Issler, 1993). Cylindrical pore shapes are assumed to characterize the pore system in mudrock (Katsube and Issler, 1993) and mudrock saprolite, and therefore

$$d = (-4\gamma \cos\theta) / p \qquad (1)$$

d = throat size
γ = interfacial (surface) tension (for Hg/vacuum = $0.48 N \cdot m^{-1}$)
θ = contact angle (for Hg/vacuum = 30°)
p = intrusion pressure (MPa).

With the help of the Washburn Equation a corresponding pore-throat size can always be *calculated* from a *measured* injection pressure.

Procedure. Prior to the petrophysical measurements the specimens were dried in a vacuum oven at a temperature of 105°C for 24 h. Following oven drying the specimens were cooled in a desiccator.

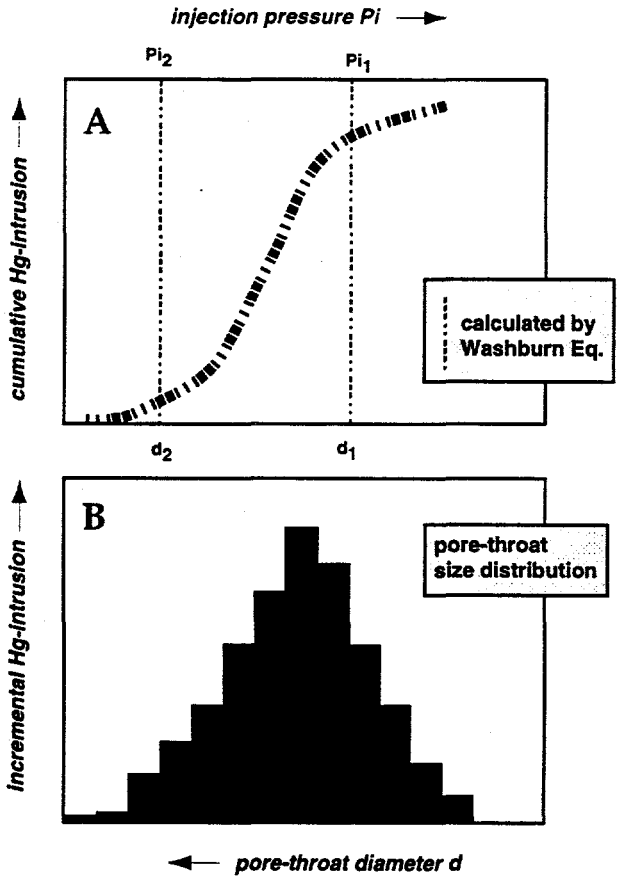

Fig. 4: Capillary-pressure curves, plotting the measured injection pressure and/or the calculated pore-throat diameter versus the amount of intruded mercury (arrows point toward higher values).
A) cumulative intrusion curve, where the total amount of intruded mercury can be read at the right-side end of the curve; d_1 and d_2 are pore-throat diameters calculated from intrusion pressures Pi_1 and Pi_2 using the Washburn Equation.
B) incremental intrusion curve showing the amount of mercury intruded at the chosen consecutive pressure steps. Note the pore-throat size distribution obtained in this way (from Dorsch, 1995).

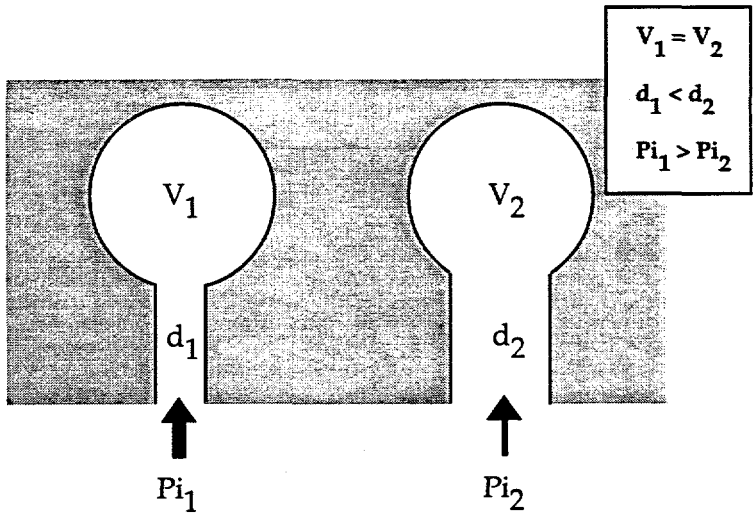

Fig. 5: Illustration of the importance of pore throats for controlling access to pores. Pores of the same size (V = volume) are accessed by pore throats of different sizes (d = diameter); mercury enters the pore throat only after an injection pressure (= Pi) is reached to force mercury through the pore throat. The pore accessed by the larger pore throat will be invaded earlier at a lower injection pressure than the pore of equal size but with a smaller entry pore-throat (from Dorsch, 1995).

A Micromeritics Autopore 9200 porosimeter was employed for the petrophysical measurements. This mercury porosimeter can generate pressures from 0.14 to 420 MPa, which corresponds to an equivalent pore-throat size ranging from 10 to 0.003 µm (10000 to 3 nm). A measurement accuracy for volume of intruded mercury of ±0.0015 cm^3 or smaller can be expected (Kopaska-Merkel, 1991).

During the petrophysical measurements the mercury-injection pressure was increased successively in discrete steps (56 steps from 0.14 to 420 MPa), equally dividing the available pressure range provided by the apparatus on a logarithmic scale. Following each step, time is allotted for equilibration of the system so that no change in volume of mercury taken up by the specimen with time occurs. Equilibrium times were about 40 s for high pressure steps (> 0.7 MPa) and 10 s for low pressure steps (< 0.7 MPa) (Katsube and Issler, 1993). For each pressure step the volume of mercury intruding the sample is recorded. Based on the Washburn Equation each discrete pressure step corresponds to a certain pore-throat size. The volume of mercury

intruding the specimen at each discrete pressure step is converted into the porosity for that pore-throat size and for pores accessed through pore throats of that size (Katsube and Issler, 1993).

Effective Porosity. The effective porosity of the specimen (ϕ_{Hg}) can be determined by summing up all partial porosity values. Partial porosity ϕ_a refers to the porosity contributed by each chosen range of pore-throat sizes (Katsube and Best, 1992). Partial porosity ϕ_a is calculated for each pore-size range by using the volume of the intruded mercury at this size range and the bulk volume of the sample. The bulk-sample volume was determined with calculations involving the penetrometer (sample chamber) volume and its weight (with mercury, with sample and mercury). Katsube and Issler (1993) split ϕ_{Hg} into a ϕ_{Hg1} (sum of all ϕ_a from pore sizes ≤10 μm) and a ϕ_{Hg2} (sum of all ϕ_a from pore sizes ≤250 μm). The reason for this split is that ϕ_{Hg2} might contain measurement errors induced by the space left between sample and penetrometer wall. ϕ_{Hg1} is more likely to reflect true effective porosity of the sample for pore sizes of 3 to 10000 nm.

Tabulation of partial porosities provides the distribution of pore-throat sizes for the analyzed specimen. Pore-throat-size data are grouped into size classes, with each decade of the logarithmic pore-throat-size scale being subdivided into 5 size ranges of equal physical spacing (Katsube and Issler, 1993; Katsube and Williamson, 1994).

Geometric Mean of Pore-Throat Sizes. In addition to effective porosity and the range of pore-throat sizes, the geometric mean of the entire pore-throat-size distribution of a specimen can be calculated using the equation (Katsube and Issler, 1993)

$$\log (d_{Hg}) = \frac{(1/n) \sum_{i=1}^{n} [\phi_{ai} \cdot \log (d_{ai})]}{\sum_{i=1}^{n} \phi_{ai}} \qquad (2)$$

ϕ_a = partial effective porosity
d_{Hg} = geometric mean of the entire pore-throat-size distribution
d_a = geometric mean of distinct pore-size range
n = number of distinct pore-size ranges.

Helium Porosimetry

Principle. Helium porosimetry is based on the Boyle-Mariotte Law. A change in gas volume or gas pressure causes a commensurate change in gas pressure or volume, given that the temperature remains constant. Important for helium porosimetry is that an increase in available space causes the gas to expand resulting in the decrease in gas pressure (American Petroleum Institute, 1960; Luffel and Howard, 1988).

Procedure. Prior to the petrophysical measurements, the specimens were dried in a vacuum oven at a temperature of 105°C for 24 h. Following oven drying the specimens were cooled in a desiccator.

For helium porosimetry the specimen is placed into a steel chamber of known volume. Helium isothermally expands into the chamber from a reservoir of known volume and pressure until equilibrium pressure is reached (30 min to 1 h). From the new gas pressure the grain volume can be calculated. The bulk volume of the sample is then determined by immersion of the specimen in mercury (measuring volume of mercury displaced from a pycnometer, or measuring the buoyant force, based on the Archimedes principle).

Effective Porosity. Effective porosity is calculated by subtracting the grain volume from the bulk volume, and dividing the result by the bulk volume of the specimen.

$$\phi_{He} = (V_{bimm} - V_g) / V_{bimm} \qquad (3)$$

ϕ_{He} = effective porosity (determined with helium porosimetry)
V_g = grain volume
V_{bimm} = bulk specimen-volume measured with mercury immersion.

SAMPLING

Cores

Saprolite specimens for the petrophysical measurements were obtained from coreholes drilled into the Whiteoak Mountain thrust sheet on the ORR. The drill site is situated within Bear Creek Valley (Figure 6) along strike to the southeast of the Y-12 Plant. Core material was available from coreholes GW-821, GW-822, and GW-823. The coreholes were drilled in June of 1994 using Rotasonic dry drilling for the regolith interval (soil and saprolite) and rotary drilling with water for bedrock (Moline and Schreiber, 1995). The cores are nearly complete and undisturbed through the saprolite mantle and are described in detail by Schreiber (1995) and Moline and Schreiber (1995). The cores were laid out in sequence with increasing depth in Building 7042 ('core barn') at X-10 for sampling. The soil zone in the cores is thin and reaches to about 15 cm below the ground surface (Schreiber, 1995; M. Elless, pers. comm.).

Sampling Intervals

The cores were inspected and sampling intervals were chosen (Figure 7) based on the following criteria: 1) incorporation of the complete weathering zone above bedrock, 2) availability of multiple macroscopically homogeneous specimens (analysis specimens; duplicate specimens for use in case of analysis-specimen failure), 3) absence of excessive deformation, and 4) availability of appropriate lithologies (groundmass and mudrock fragments, see below). Sampling intervals for saprolite groundmass were generally ≤ 7 cm in length, whereas sampling intervals for saprolite mudrock-fragments were generally ≤ 15 cm in length. The code for the sampling intervals includes the corehole designation followed by an interval number (e. g., GW-823-7). The interval number is based on sequentially numbering the core intervals as used by Schreiber (1995) and Moline and Schreiber (1995) for core description. Appendix I provides an overview of sampling intervals, their code, drill depth (the median of the chosen sampling interval is used), and specimen type. Overall, 10 sampling intervals were selected from cores GW-822 and GW-823.

Saprolite Specimens

Specimens for petrophysical analysis were selected from the chosen sampling intervals, with each sampling interval providing one specimen pair for analysis (one

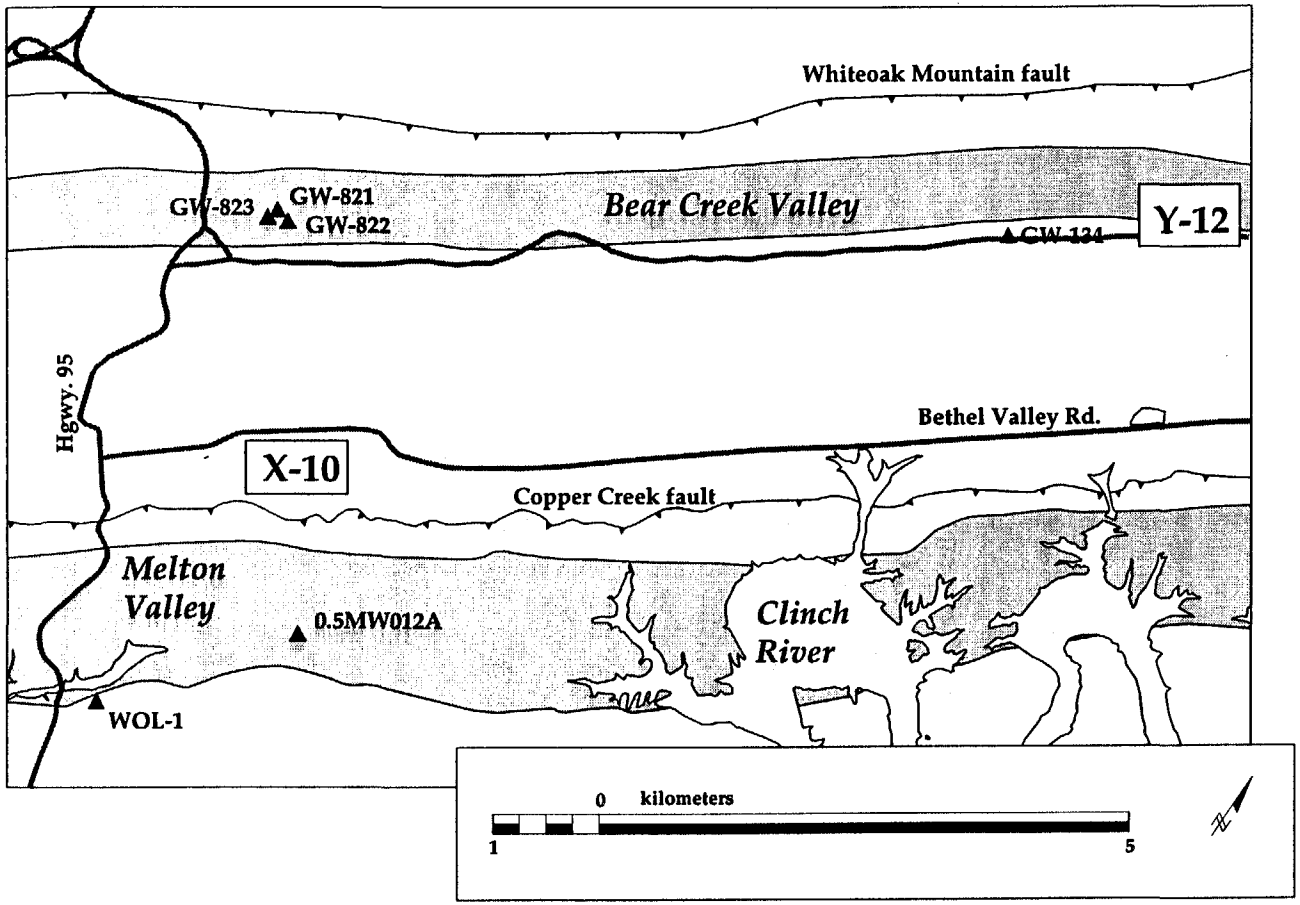

Fig. 6: Generalized location map. Dark stippled bands traversing the ORR outline the mudrock-dominated part of the Conasauga Group in outcrop. Barbed solid black lines indicate the location of the Whiteoak Mountain fault and of the Copper Creek fault, whereas stippled lines indicate major roads. Triangles refer to the location of coreholes from which specimens were selected: GW-821, -822, -823 for mudrock saprolite of the Nolichucky Shale, corehole GW-134 for mudrock (bedrock) of the Nolichucky Shale.
(modified from Dorsch et al., 1996; based on Hatcher et al., 1992).

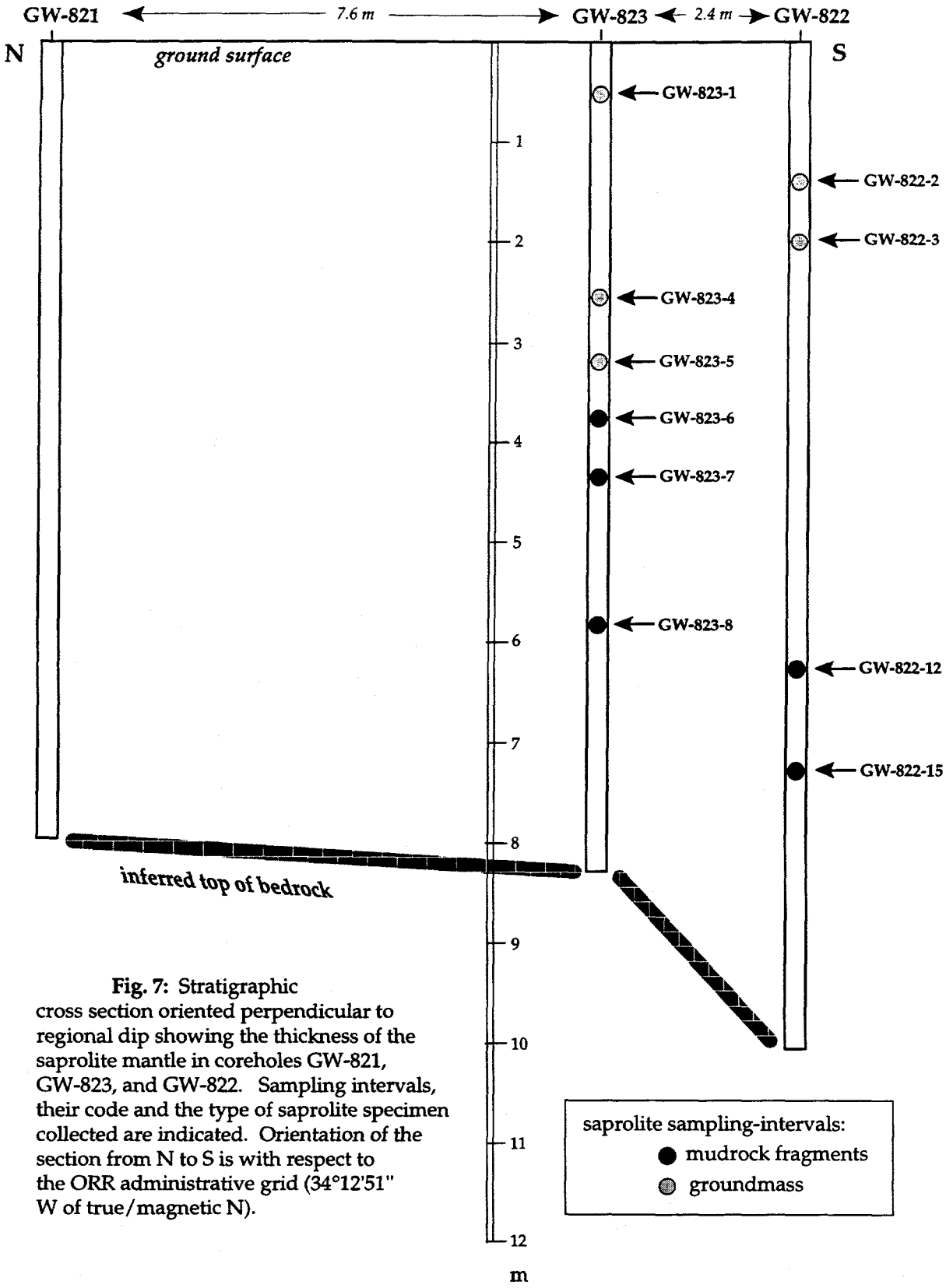

Fig. 7: Stratigraphic cross section oriented perpendicular to regional dip showing the thickness of the saprolite mantle in coreholes GW-821, GW-823, and GW-822. Sampling intervals, their code and the type of saprolite specimen collected are indicated. Orientation of the section from N to S is with respect to the ORR administrative grid (34°12'51" W of true/magnetic N).

specimen for helium porosimetry and one specimen for mercury porosimetry) and additional duplicate specimens for use in case of analysis-specimen failure. All specimens were of irregular shape. Overall, a total of 20 specimens were analyzed (10 each with mercury and helium porosimetry).

The saprolite cores were divided into two components: 1) groundmass, and 2) sedimentary rock fragments. Groundmass consists of heavily weathered mudrock material which still has coherence and shows original sedimentary and tectonic structures. Saprolite groundmass is plastic and easily deformable when moist or wet, and is friable and crumbly when dry. The groundmass constitutes most of the saprolite mantle and contains more rigid and harder, well defined sedimentary rock fragments. The vast majority of these "floating" fragments are mudrock, but also a few small siltstone/fine sandstone and rare larger limestone fragments were encountered. The mudrock fragments are similar to mudrock (bedrock) in appearance, but are noticeably softer when scratched with a knife. It was often observed that a larger piece of saprolite groundmass contained a more solid and harder mudrock fragment in its center, after the friable groundmass mantle was crumbled away.

Mudrock-Fragment Specimens. Mudrock[1] fragments for analysis were pulled directly out of the moist saprolite groundmass. In the laboratory, the surface-dry fragments were carefully cleaned using dry and slightly damp kimwipe® tissues, a toothbrush, and a small knife. No water was used for specimen cleaning (note: earlier sampled material was cleaned under running tap water, but this caused the mudrock fragments to become too fragile and the procedure was then discontinued). The mudrock-fragment specimens were ≤10 g. Ten specimens were used for petrophysical analysis, with 57 additional specimens retained as duplicates for use in case of analysis-specimen failure.

Groundmass Specimens. Groundmass specimens for analysis were retrieved from core segments ≤7 cm in length. The segments were predominantly moist at the time of sampling but also two dry segments were used. The segments were put into an oven for

[1] mudrock refers to all types of fine-grained siliciclastic rock, following the definition of Blatt et al. (1980); however, sampled material for petrophysical analysis (saprolite and bedrock) were predominantly mudstone and claystone, with subordinate mud-shale and clay-shale; no siltstone, silt-shale, or marlstone specimens were used for analysis.

48 h and dried at a temperature of 60°C. The result were dry and hardened but still brittle and friable core segments of saprolite groundmass. The core segments were then carefully broken into smaller coherent units using pliers, a knife and a screw driver. The smaller units were then prepared to size and cleaned under a laboratory hood using dry kimwipe® tissues, toothbrush, and knife. No water was used for specimen cleaning. The groundmass specimens were ≤8.55 g. Specimens with macroscopic cracks were discarded. All saprolite-groundmass specimens represent small coherent units devoid of visible cracks and fractures. Ten specimens were used for petrophysical analysis, with eleven additional specimens and several core segments retained as duplicates for use in case of analysis-specimen failure.

GRAIN-DENSITY AND BULK-DENSITY DATA

Specimen Bulk-Density

Bulk-density data was obtained for the saprolite specimens by mercury porosimetry. The results are displayed in Table 1 and shown in a scatter plot (Figure 8).

Saprolite mudrock-fragments display an arithmetic mean of 2.44 (± 0.07) $g \cdot cm^{-3}$ (Appendix II). The values range from a minimum of 2.36 $g \cdot cm^{-3}$ to a maximum of 2.53 $g \cdot cm^{-3}$. The scatter of the data, as apparent from Figure 8, is small.

The results for the *saprolite-groundmass specimens* are markedly different, however. All values are below 2.00 $g \cdot cm^{-3}$, with a minimum of 1.48 $g \cdot cm^{-3}$ and a maximum of 1.91 $g \cdot cm^{-3}$ (Table 1). The arithmetic mean is 1.75 (± 0.19) $g \cdot cm^{-3}$ (Appendix II). The scatter of the data is considerably larger than the scatter for the saprolite mudrock-fragments (Figure 8).

Table 1: Data on specimen grain density δ_{He} and specimen bulk-density δ_{Hg} for mudrock-saprolite specimens, Bear Creek Valley on the ORR.

sampling interval	δ_{He} [$g \cdot cm^{-3}$]	δ_{Hg} [$g \cdot cm^{-3}$]	specimen type
GW-822-12	2.81	2.50	mudrock fragment
GW-822-15	2.81	2.53	mudrock fragment
GW-823-6	2.78	2.36	mudrock fragment
GW-823-7	2.78	2.39	mudrock fragment
GW-823-8	2.80	2.40	mudrock fragment
GW-822-2	2.90	1.81	saprolite groundmass
GW-822-3	2.87	1.92	saprolite groundmass
GW-823-1	2.76	1.48	saprolite groundmass
GW-823-4	2.70	1.64	saprolite groundmass
GW-823-5	2.72	1.91	saprolite groundmass

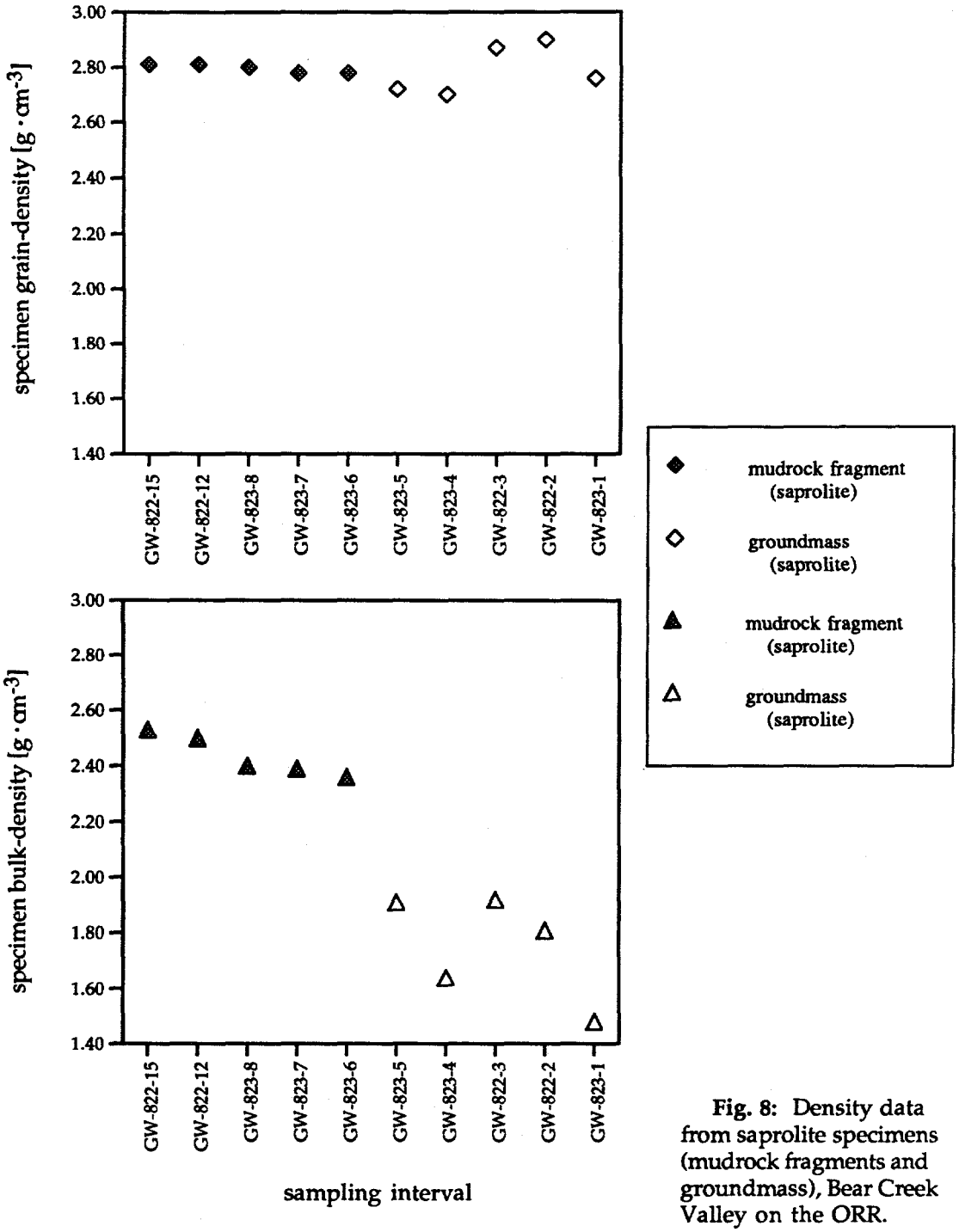

Fig. 8: Density data from saprolite specimens (mudrock fragments and groundmass), Bear Creek Valley on the ORR.

Specimen Grain-Density

The data on grain density were obtained during helium porosimetry for specimens from the same sampling intervals as the data for bulk density. Overall, the specimen grain-density data are higher than the specimen bulk-density data.

For *saprolite mudrock-fragments* the values range from 2.78 $g \cdot cm^{-3}$ to 2.81 $g \cdot cm^{-3}$, with an arithmetic mean of 2.80 (± 0.02) $g \cdot cm^{-3}$ (Table 1; Appendix II). The data show only a minimal scatter and are virtually identical (Figure 8).

The *saprolite groundmass-specimens* display an arithmetic mean of 2.79 (± 0.09) $g \cdot cm^{-3}$ (Appendix II) with a minimum value of 2.70 $g \cdot cm^{-3}$ and a maximum value of 2.90 $g \cdot cm^{-3}$ (Table 1). The scatter in the data is larger than for the saprolite mudrock-fragments, but is still small.

PORE-THROAT-SIZE DATA

Quantitative data on the sizes of pore throats and their distribution were obtained for all analyzed saprolite specimens by mercury porosimetry. The data are tabulated in detail in Appendix III, and the resulting pore-throat-size distribution curves for each saprolite specimen are shown in Appendix IV.

Saprolite Mudrock-Fragments

Pore-throat-size distribution curves of saprolite mudrock-fragments (Figure 9; Appendix IV) are unimodal to bimodal and are skewed to the right (steeper slopes toward smaller throat sizes together with long and gentle slopes toward larger throat sizes). The pore-throat-size distributions show zero values at the higher end of the tested size spectrum and terminate abruptly at about 3 nm at the lower end of the tested size spectrum (Figure 9, Appendices III, IV). Therefore, the smallest pore-throat sizes encountered are in the size class with a mean of 3.2 nm, whereas the largest pore-throat sizes are in the size classes characterized by means of 794 nm, 1259 nm, and 3162 nm (there can be smaller outliers) (Figure 9; Appendix III). The modes of the distribution curves reside within different size classes for different specimens, but fall consistently between 5 nm and 20 nm. The geometric means for the entire pore-throat-size distribution of saprolite mudrock-fragments are very similar and range from 18 to 28 nm (Appendix III). It is apparent from the distribution curves that the vast majority of the pores are accessed by pore throats smaller than 100 nm in size (Figure 9; Appendix IV).

Saprolite Groundmass

Pore-throat-size distribution curves of saprolite-groundmass specimens (Figure 9; Appendix IV), in contrast, are skewed toward the left (steeper slopes toward larger throat sizes with long and gentle slopes toward smaller throat sizes). Distribution curves commonly are unimodal (with smaller secondary modes) with pronounced modes

Fig. 9: Typical pore-throat-size distribution curves for saprolite developed from mudrock of the Nolichucky Shale, Bear Creek Valley on the ORR. Vertical axis shows partial effective porosity in %, horizontal axis shows size of pore throats in nanometers. A, B, C show curves for saprolite mudrock-fragments, D and E show curves for saprolite-groundmass specimens.

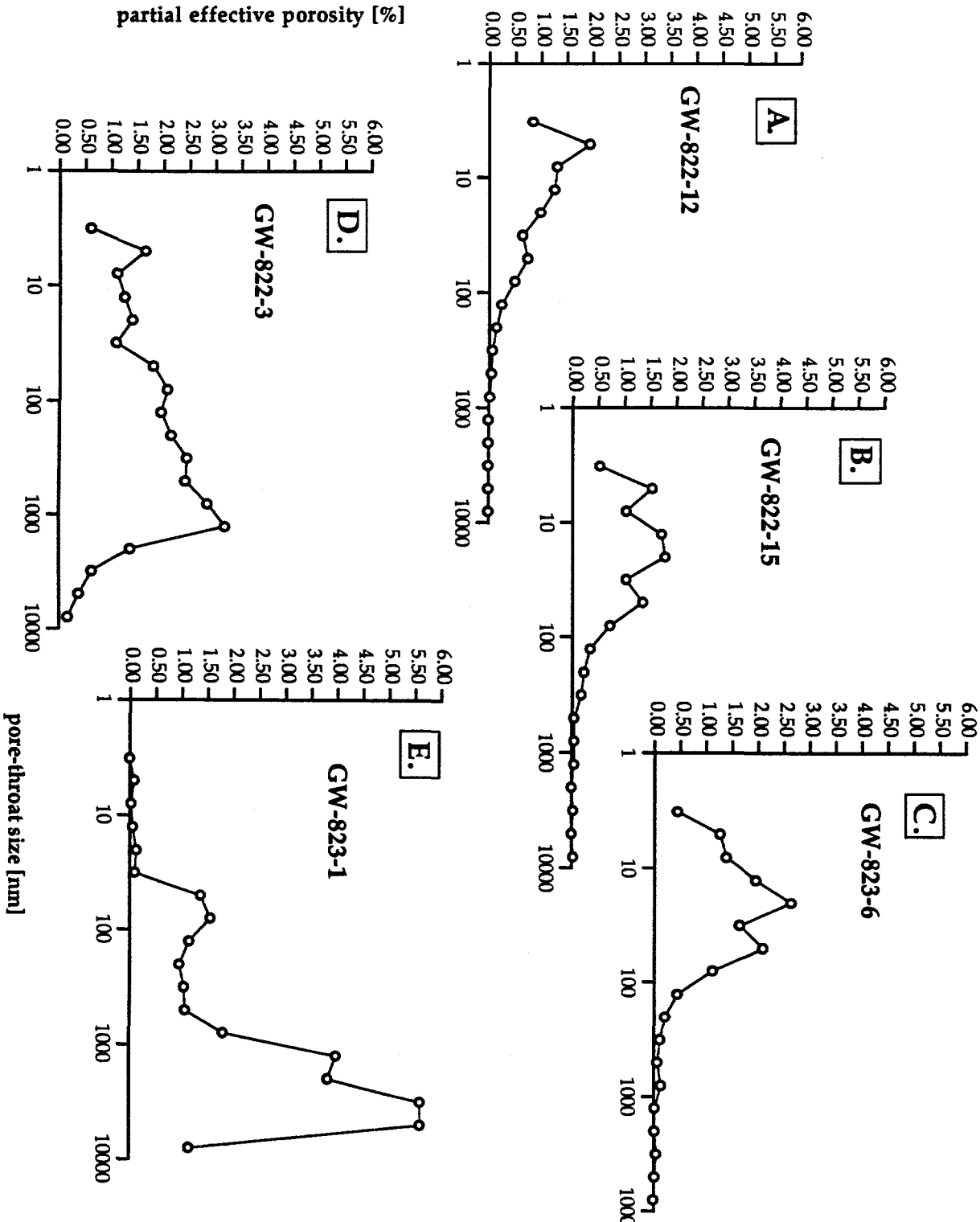
A.
GW-822-12
B.
GW-822-15
C.
GW-823-6
D.
GW-822-3
E.
GW-823-1
partial effective porosity [%]
pore-throat size [nm]
0.00
0.50
1.00
1.50
2.00
2.50
3.00
3.50
4.00
4.50
5.00
5.50
6.00
1
10
100
1000
10000

(Appendix IV). The modes reside within the size class with a mean of 1259 nm, with one example displaying the mode between 3000 and 5000 nm (Appendix III). Geometric means for the entire pore-throat-size distribution of saprolite-groundmass specimens are considerably higher than for saprolite mudrock-fragments and show a wide variation. The values range from 182 to 2201 nm, with the vast majority of the values being above 850 nm. The smallest pore-throat sizes encountered are in the size class with the mean of 3.2 nm (one exception with 7.9 nm), as was the case for saprolite mudrock-fragments (Figure 9; Appendices III, IV). At the higher end of the analyzed size spectrum, however, no zero values are reached and the curves appear to terminate abruptly at the reported size class with 7943 nm as a mean. The curves show that the vast majority of the pores are accessed by pore throats larger than 100 nm in size, in direct contrast to the data reported for saprolite mudrock-fragments (Figure 9; Appendix IV).

EFFECTIVE POROSITY DATA

Helium Porosimetry

Effective porosity values for saprolite specimens determined with helium porosimetry are shown in Table 2. The accuracy of the measurements is estimated to be within 10 to 20% of the measured value.

For *saprolite mudrock fragments* the values range from 13.5 to 18.1%, with a mean of 16.1 (±1.8)% (Table 2; Appendix II). The scatter of the data is very small (Figure 10).

The values obtained for *saprolite-groundmass specimens*, in contrast, are markedly higher with a minimum of 31.7% and a maximum of 51.6% (Table 2). The data also display a considerably larger scatter, with a mean of 39.0 (± 7.5)% (Figure 10; Appendix II).

Table 2: Data on effective porosity of saprolite specimens; ϕ_{He} refers to data obtained with helium porosimetry, whereas ϕ_{Hg} refers to data obtained with mercury porosimetry (Hg1: for pore throats ≤10 µm, Hg2: for pore throats ≤250 µm).

sampling interval	ϕ_{He} [%]	ϕ_{Hg1} [%]	ϕ_{Hg2} [%]	specimen type
GW-822-12	16.7	8.8	9.2	mudrock fragment
GW-822-15	13.5	10.7	11.2	mudrock fragment
GW-823-6	18.1	13.7	14.0	mudrock fragment
GW-823-7	15.1	12.2	12.8	mudrock fragment
GW-823-8	17.3	9.5	10.1	mudrock fragment
GW-822-2	38.9	22.0	23.7	saprolite groundmass
GW-822-3	33.6	28.5	29.3	saprolite groundmass
GW-823-1	51.6	29.5	37.5	saprolite groundmass
GW-823-4	39.3	26.7	38.2	saprolite groundmass
GW-823-5	31.7	27.2	40.0	saprolite groundmass

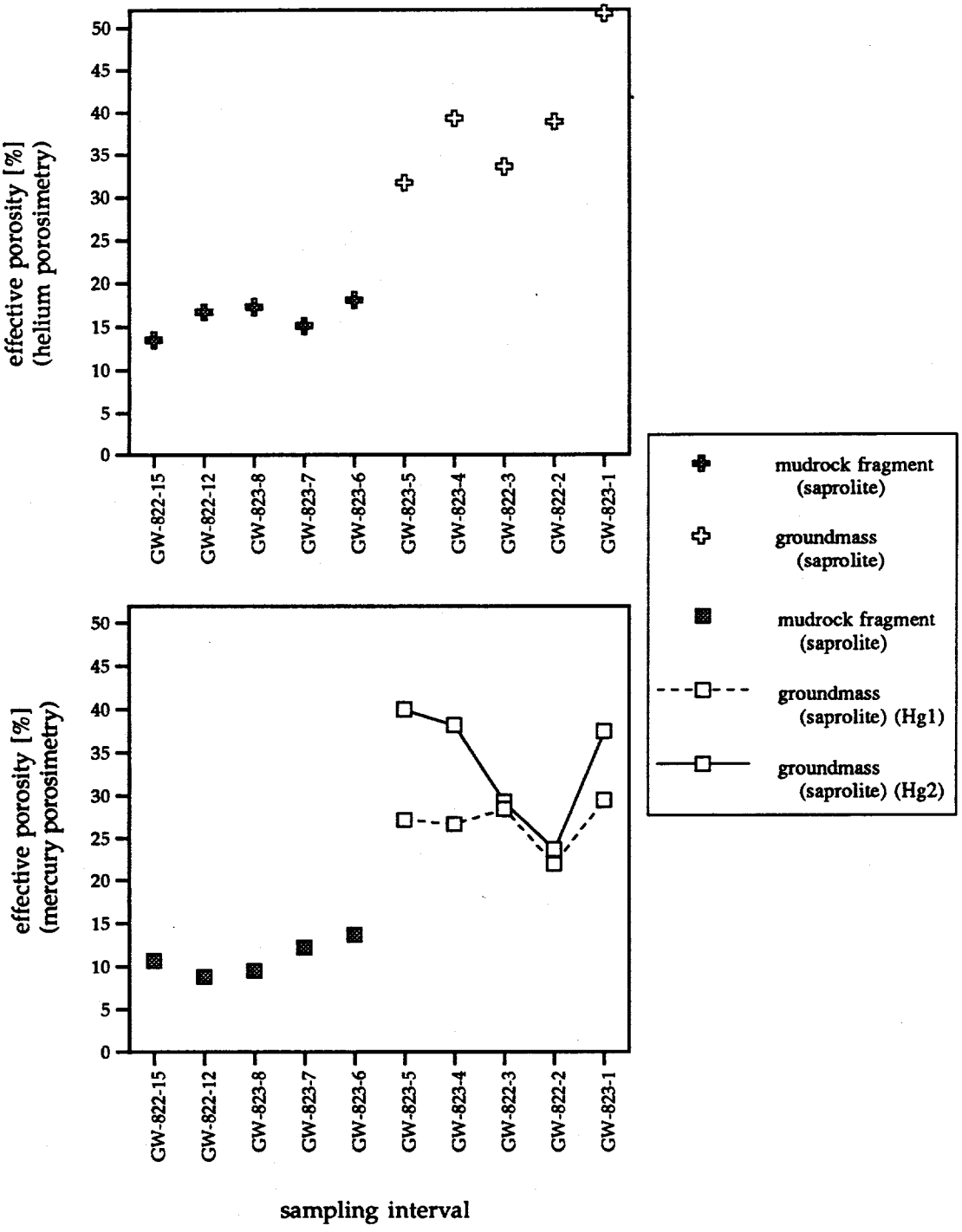

Fig. 10: Effective porosity data from saprolite specimens (mudrock fragments and groundmass), Bear Creek Valley on the ORR. Helium-porosimetry data are shown in the upper graph, mercury-porosimetry data are shown in the lower graph.

Mercury Porosimetry

Effective porosity data obtained with mercury porosimetry are reported in two forms (Table 2). Hg1-data refer to pores accessed by pore throats ≤10000 nm, whereas Hg2-data include pores accessed by pore throats ≤250000 nm. Hg1-data are commonly judged as more reliable because they are less likely to include measurement errors than Hg2-data (Katsube and Issler, 1993). Hg1-data are used for saprolite mudrock-fragments. The shift of the pore-throat size spectrum toward larger sizes for saprolite groundmass (see above) makes it advisable, however, to use Hg2-data for the saprolite-groundmass specimens. This entails the possibility, though, that added effective porosity is incorporated due to measurement errors. The small difference between Hg1-values and Hg2-values for saprolite mudrock-fragments (Table 2) indicates that most pore space is characterized by entry pore-throats ≤10000 nm in size. Two specimens of saprolite groundmass (GW-822-2, GW-822-3) show similarly small differences, again indicating that most interconnected pore space is accessed by pore throats <10000 nm in size. The larger differences between Hg1-values and Hg2-values for some saprolite-groundmass specimens (GW-823-1, GW-823-4, GW-823-5) (Table 2; Figure 10) simply reflect that a significant portion of pores are accessed by pore-throats in excess of 10000 nm. Hg1-data are plotted for saprolite mudrock-fragments in Figure 10, whereas both Hg1- and Hg2-data are shown for saprolite-groundmass specimens, with Hg2-data considered to more likely reflect true effective porosity (see further discussion below). As for helium porosimetry, the accuracy of the measurements is estimated to be within 10 to 20% of the measured value.

Saprolite mudrock-fragments show a mean effective porosity of 11.0 (± 2.0)%, with minimum and maximum values of 8.8% and 13.7%, respectively (Table 2; Appendix II). The scatter of the data is small (Figure 10).

Effective porosity data (Hg2) for *saprolite-groundmass specimens*, on the other hand, are considerably larger, ranging from 23.7 to 40.0%, with a mean of 33.7 (± 7.0)% (Table 2; Appendix II). The scatter of the data, furthermore, is considerably larger than for effective porosity data of saprolite mudrock-fragments (Figure 10). Hg1 effective porosity data show maximum and minimum values of 29.5% and 22.0%, with a mean of 26.8 (±2.9)% (Table 2; Appendix II).

Calculated Interval Effective Porosity

The saprolite mantle above bedrock is characterized by heavily weathered saprolite groundmass which contains less weathered fragments (mostly mudrock). For selected intervals of the saprolite mantle (Figure 11), matrix effective porosities were calculated using helium-porosimetry data. These calculations are based on:

1) using the *measured* effective porosity value of the analyzed specimen type from the selected sampling interval (either saprolite mudrock-fragment or saprolite groundmass effective porosity),

2) *assuming* the complementary effective porosity value for the specimen type not analyzed from the selected sampling interval (either saprolite groundmass or saprolite mudrock-fragment effective porosity), and

3) estimating the relative proportion of the two saprolite specimen-types (groundmass and mudrock-fragment) over the length of the chosen sampling interval.

From the relative proportion of mudrock fragments and groundmass and their effective porosities, the interval effective porosity can be calculated. The data used for the calculation of interval effective porosities are provided in Appendix V.

As an example, consider saprolite sampling-interval GW-823-4. It is composed to approximately 97% of groundmass and to 3% of mudrock-fragments (Appendix V). A measured effective porosity value of 39.3% is available for the groundmass of this sampling interval. A complementary effective porosity value for mudrock fragments is not available and must be assumed. A value of 18.1% was chosen, because this is the highest measured mudrock fragment effective porosity value from sampling zones below sampling interval GW-823-4. This value is interpreted to best approximate the effective porosity of saprolite mudrock-fragments within sampling interval GW-823-4. The two effective porosity values are then multiplied by the estimated respective proportions of the specimen types within the chosen sampling interval, resulting in an effective porosity contribution of 38.12% from saprolite groundmass and of 0.54% from saprolite mudrock fragments. Adding up the two values finally provides the effective porosity of the saprolite matrix of the chosen sampling interval of 38.7% excluding macroscopically visible fractures.

Note that there also can be carbonate-rock fragments (predominantly rare, but up to 10% in one interval) within the saprolite groundmass. The observed carbonate-rock fragments, however, are fresh, hard and "tight" indicating low levels of effective porosity. Because of their "tightness" and scarcity they are judged to be a negligible

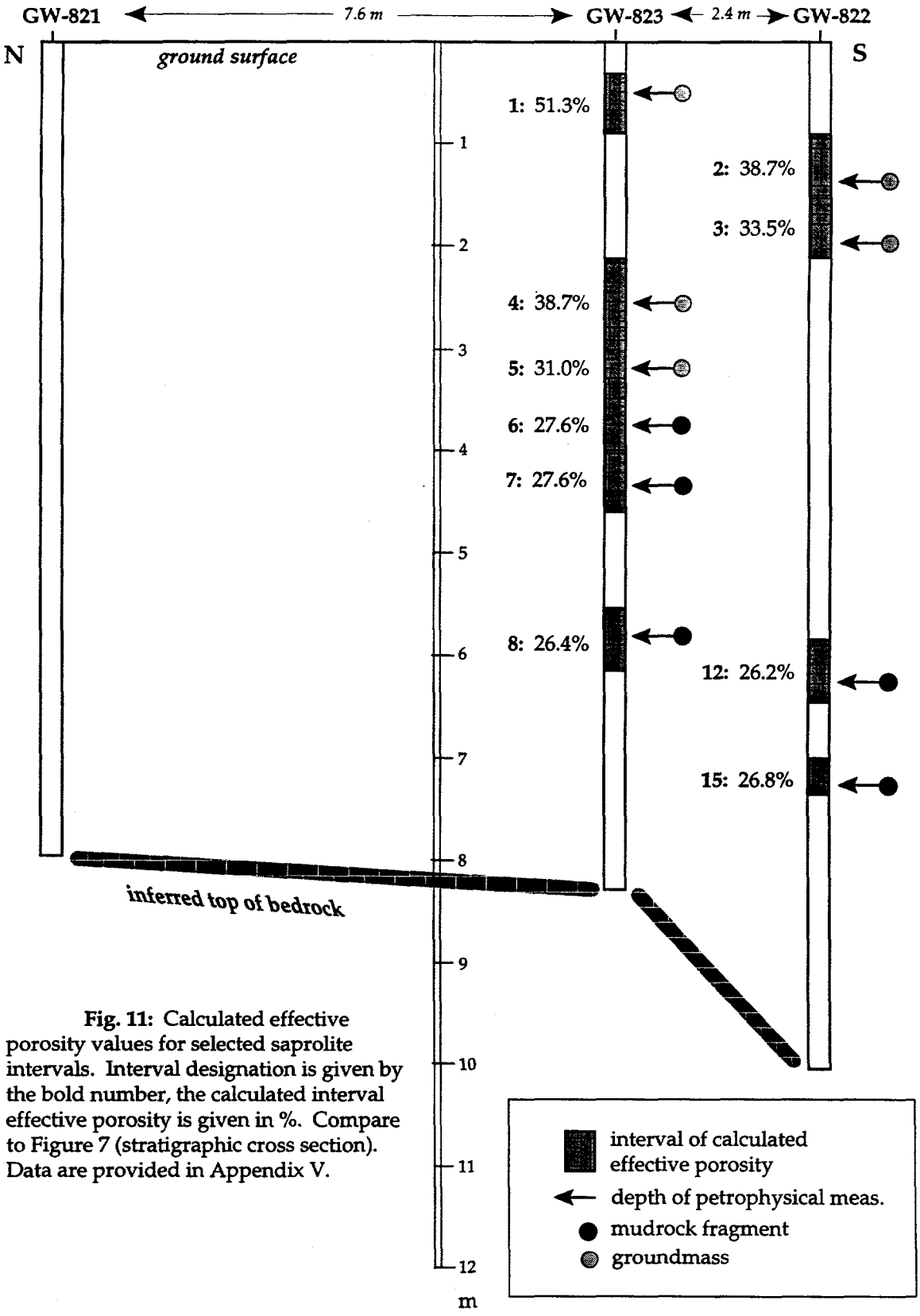

Fig. 11: Calculated effective porosity values for selected saprolite intervals. Interval designation is given by the bold number, the calculated interval effective porosity is given in %. Compare to Figure 7 (stratigraphic cross section). Data are provided in Appendix V.

addition to overall saprolite-matrix effective porosity.

The results show that effective porosities of saprolite matrix for the chosen intervals range from a maximum 51.3% to a minimum of 26.2% (Figure 11; Appendix V).

COMPARISON TO BEDROCK AND DISCUSSION

The discussion section will include a comparison of the saprolite petrophysical data with petrophysical data obtained for bedrock specimens from the Nolichucky Shale within Bear Creek Valley (Dorsch et al., 1996). The Nolichucky Shale within Bear Creek Valley represents the parent material of the mudrock saprolite analyzed for this report. Bedrock petrophysical data are summarized in Appendix VI.

Specimen-Density Data

Grain-Density Data. Grain-density data for mudrock specimens from bedrock (Nolichucky Shale) display a mean of 2.77 (± 0.03) $g \cdot cm^{-3}$ (Appendix II). These values and their negligible scatter are essentially identical to the values reported for saprolite mudrock-fragments (2.80 [± 0.02] $g \cdot cm^{-3}$) (Figure 12). Furthermore, the arithmetic mean for saprolite groundmass-specimens (2.79 [± 0.09] $g \cdot cm^{-3}$) conforms to the means for mudrock fragments (bedrock and saprolite) (Appendix II). The scatter for groundmass specimens, however, is larger, although it is still small. This noticeable increase in scatter is interpreted to reflect the more severe chemical weathering experienced by the saprolite groundmass. The two grain-density values for saprolite groundmass above the normal trend (GW-822-3, GW-822-2) might indicate the addition of more dense mineral phases or the loss of some less dense mineral phases, again reflecting the influence of chemical weathering on the grain material and/or cement. At present, there is no petrographic information available to evaluate what solid material was lost or added during weathering and the development of saprolite. The most likely explanation is the addition of denser mineral phases, such as Fe-oxides and Mn-oxides. This explanation is supported by other observations within the upper, more weathered zones of saprolites developed from the Conasauga Group on the ORR (S. Y. Lee, pers. comm.). Overall, however, the solid material of the specimens appears to have remained similar for bedrock and saprolite mudrock-fragments, with some smaller changes for saprolite groundmass.

Bulk-Density Data. Bulk-density data, in contrast, fall into three distinct groups. Mudrock specimens from bedrock display the highest values with an arithmetic mean of 2.70 (±0.03) $g \cdot cm^{-3}$ and negligible scatter (Appendices II and VI). Saprolite mudrock-fragments show lower values with a somewhat larger (but still small) scatter (2.44 [±0.07] $g \cdot cm^{-3}$), and saprolite-groundmass specimens display the lowest values with a distinctly larger scatter 1.75 [±0.19] $g \cdot cm^{-3}$) (Figure 12; Appendix II). This trend toward

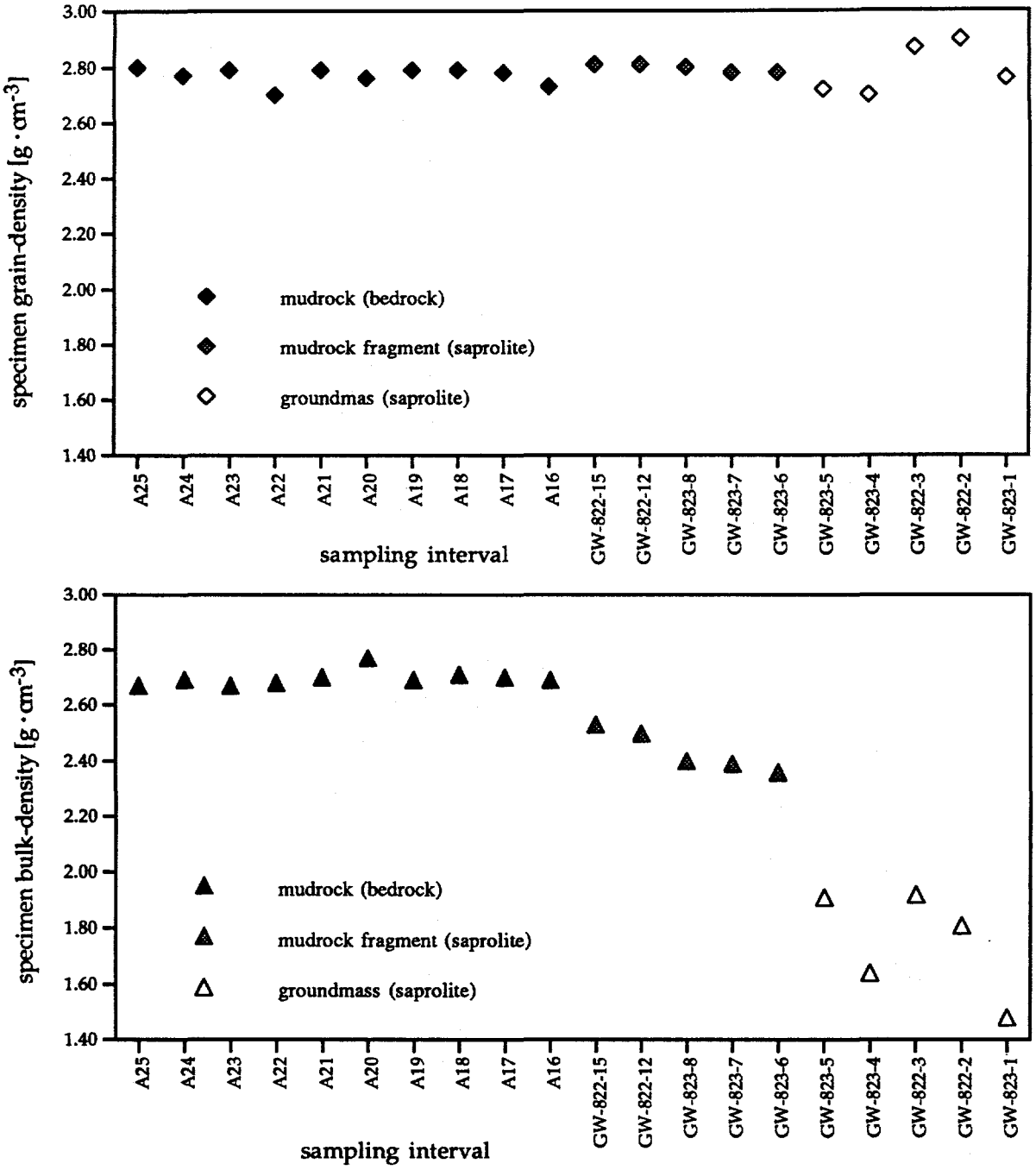

Fig. 12: Comparison of bulk and grain densities from saprolite specimens (mudrock fragments and groundmass) and Nolichucky Shale specimens (bedrock), Bear Creek Valley on the ORR.

lower bulk-density values together with enlarging scatter (Figure 12) is interpreted to reflect the increasing effect of weathering. Void space per bulk volume of specimen material expands from bedrock mudrock, through saprolite mudrock-fragments, to saprolite-groundmass specimens. The increased effect of weathering might include a loss of cement, loss of some grain material, and a loosening of the fabric. This latter aspect results in the significantly less cohesive and more friable (but still cohesive) nature of the saprolite groundmass. The most noticeable loss is probably that of carbonate cement and carbonate grains (Lietzke et al., 1992; S. Y. Lee, pers. comm.). Changes in bulk density are considerably more drastic when compared to changes in grain density, reflecting a significant increase in void space but only a comparatively less notable change in the nature of the remaining solid mineral phases.

Density Data with Depth. Density data plotted against depth (Figure 13) again show the general uniformity of the specimen grain-density values from bedrock toward the top saprolite zone. The distinct veering toward lower values for specimen bulk-density and the increased difference from grain-density data from the same sampling interval is interpreted to characterize a weathering profile from bedrock toward the shallow saprolite zones.

Pore-Throat Size Data

Mudrock specimens from the Nolichucky Shale (bedrock) from Bear Creek Valley display unimodal (rarely bimodal, with strongly weaker secondary modes) pore-throat-size distribution curves skewed toward the right. All curves terminate abruptly at about 3 nm, and the vast majority of pores is accessed by pore throats <100 nm in size (Dorsch et al., 1996; Figure 14). These characteristics match the characteristics of saprolite mudrock-fragments. The pore-throat-size distribution curves of specimens GW-822-12 and GW-823-8 especially resemble in overall shape and location of modes (5 nm size class) the pore-throat-size distribution curves of bedrock specimens (Appendix IV; Figure 14). Important differences are, however, that the area under the curves is significantly larger for saprolite mudrock-fragments than for bedrock mudrock (Figure 14). This reflects the higher effective porosities of saprolite mudrock-fragments. Commensurate with this increase in area under the distribution curves, the overall throat-size spectrum shifts to the right and toward larger throat sizes (Figure 14), exemplified by the shift of modes from 5 nm (bedrock specimens; GW-822-12, GW-823-8) to 20 nm (GW-823-7, GW-822-15, GW-823-6).

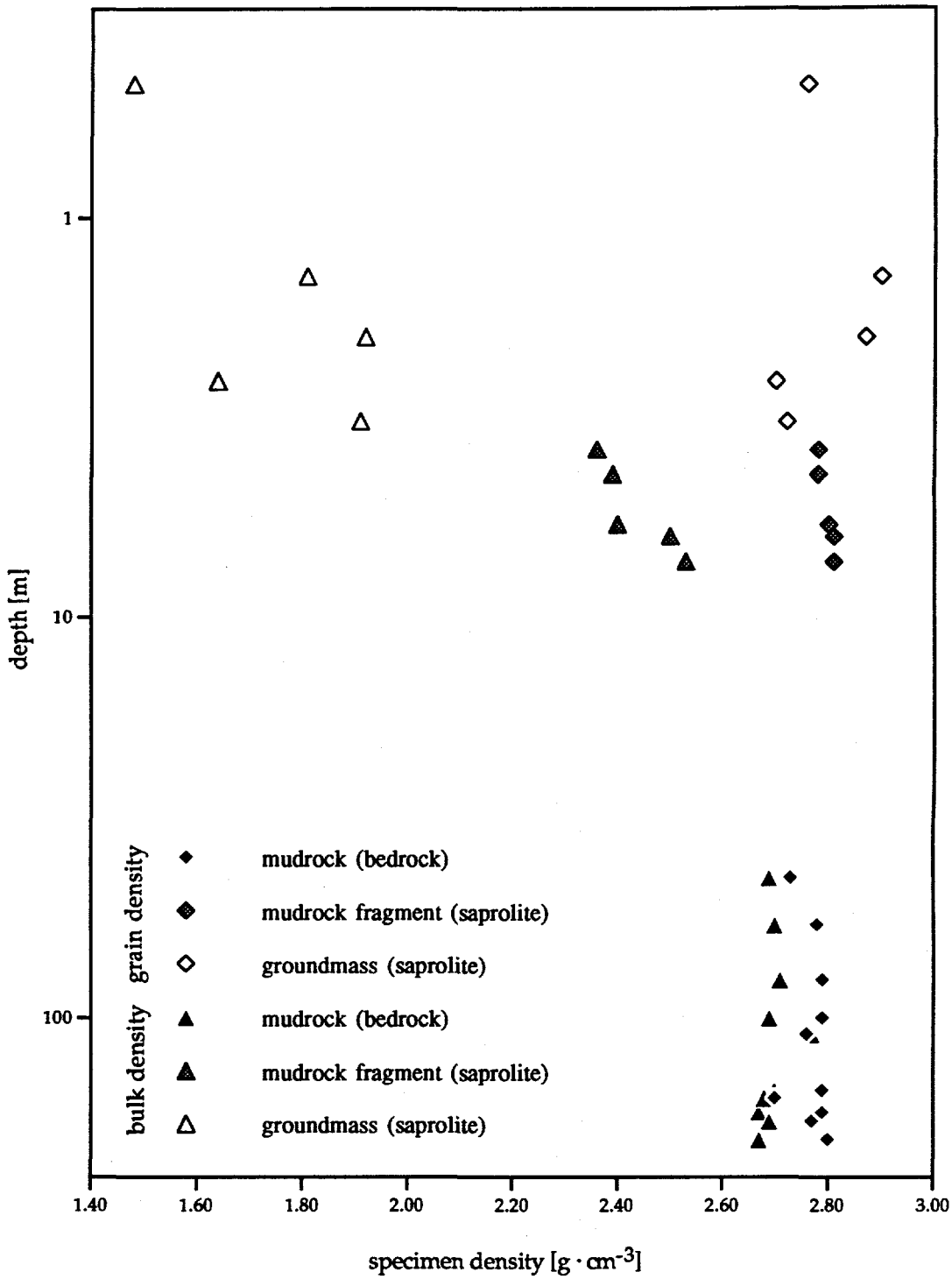

Fig. 13: Specimen density-pairs with depth for Nolichucky Shale and saprolite specimens, Bear Creek Valley on the ORR. Maximum depth is 201.19 m, minimum depth is 0.46 m; depth is given as below ground surface (note log-scale on depth axis).

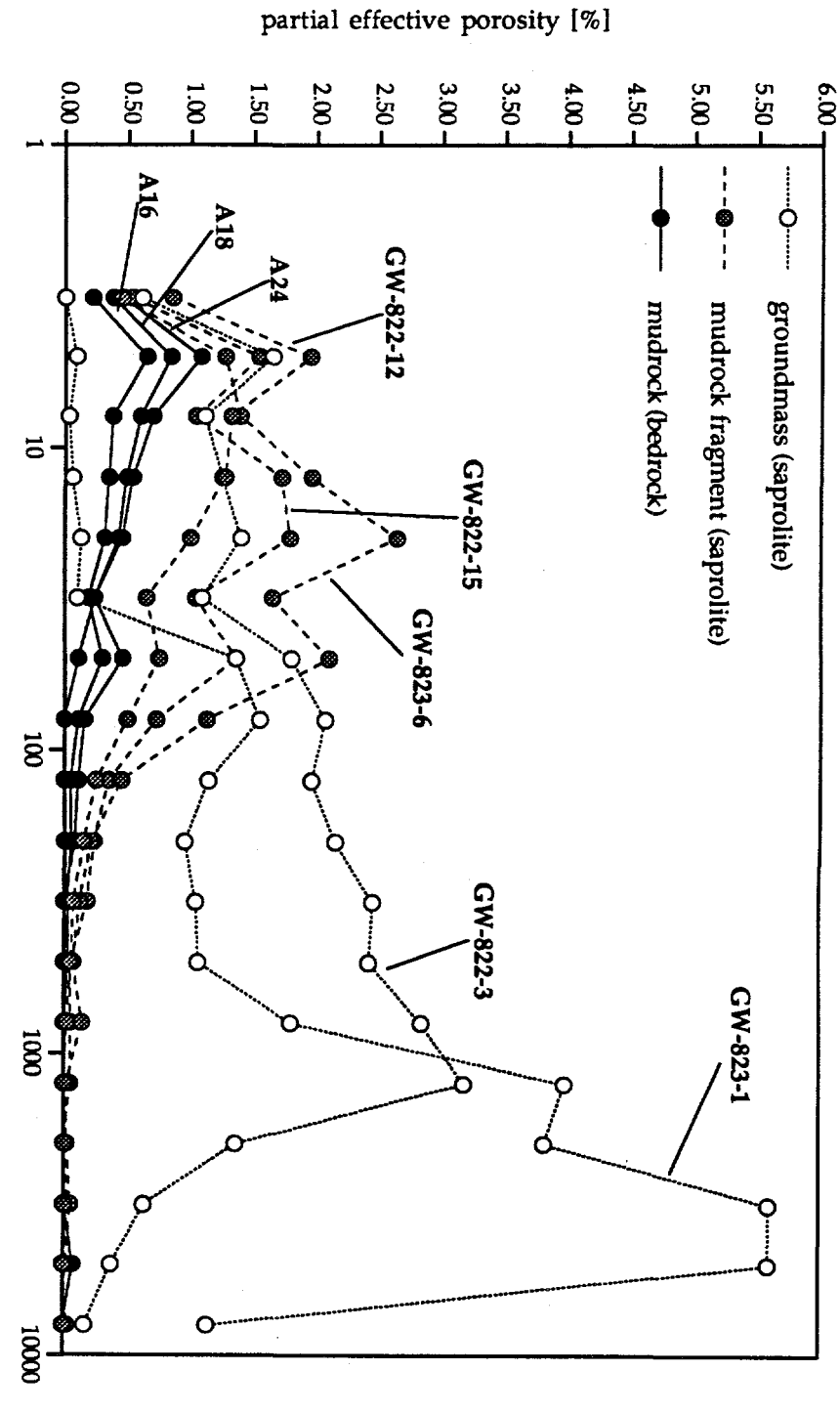

Fig. 14: Superimposed pore-throat-size distribution curves of typical saprolite (mudrock fragments and groundmass) and Nolichucky Shale (bedrock) specimens from Bear Creek Valley on the ORR.

In marked contrast to mudrock specimens (bedrock and saprolite), saprolite-groundmass specimens display pore-throat-size distribution curves which are skewed toward the left. Furthermore, the majority of pores is accessed by pore throats ≥100 nm in size (Appendix IV), and the throat-size spectrum is shifted even further to the right and toward larger throat sizes (Figure 14).

The overall shift of the pore-throat-size distribution curves to the right and toward larger throat sizes from bedrock mudrock, to saprolite mudrock-fragments, to saprolite groundmass (Figure 14) again reflects the increasing degree of changes brought on by chemical weathering. It is conceivable that cement lining pores and pore throats, clogging pore throats, and filling pores was (partially) removed during weathering, resulting in both an increase in effective porosity and an increase in the sizes of pore throats. The dissolved mineral phase was most likely carbonate cement (Lietzke, 1992; S. Y. Lee, pers. comm.).

While this observation is valid for comparing the different specimen types (bedrock, saprolite mudrock-fragments, saprolite groundmass), there are exceptions to the trend of decreasing weathering effects with depth apparent within the separate saprolite specimen-groups. For saprolite mudrock-fragments, a decrease in weathering influence might be surmised from the pore-throat-size distribution curves with depth (Figure 7), except for the anomalous character of specimen GW-822-15. This, however, might simply indicate that weathering zones have rather irregular boundaries and do not necessarily conform to parallelism with the ground surface (Figure 15; compare to Figure 2; Lietzke et al., 1988, pp. 8 to 9; see also Lee et al., 1992). The same holds true for the group of saprolite-groundmass specimens retrieved closer to the ground surface (Figure 15).

Measured data on pore-throat sizes and their distribution may be useful in evaluating whether pore throats can act to exclude or retard certain contaminant species from accessing the interconnected saprolite-matrix pore space through diffusion. Compared to mudrock specimens from bedrock (Dorsch et al., 1996), size exclusion of contaminant species appears to be of lesser significance because of the overall shift of the pore-throat size spectrum toward larger throat sizes for saprolite specimens (Figure 15). Nevertheless, small pore throats are still present within the saprolite matrix with the potential to influence contaminant transport by diffusion.

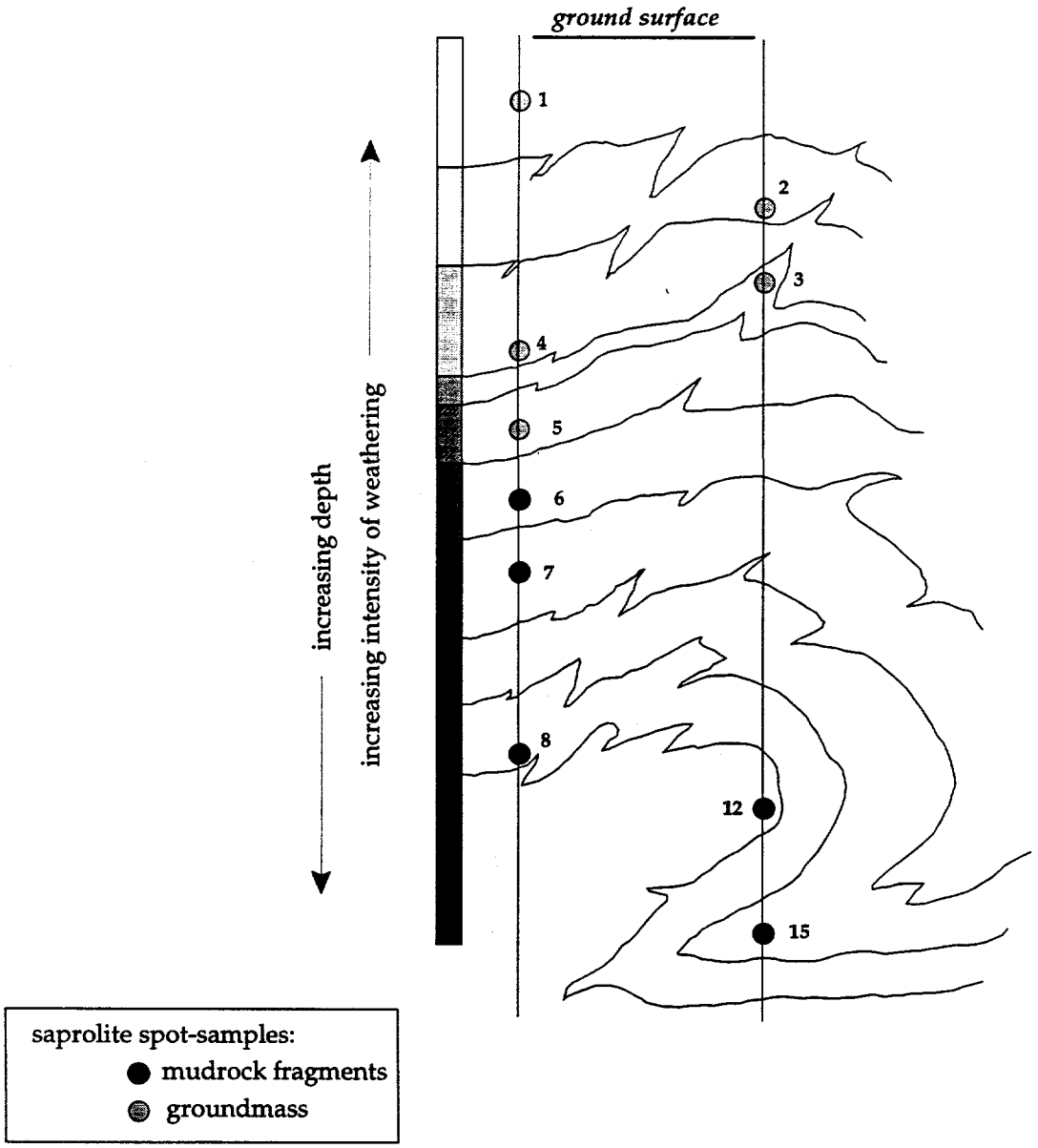

Fig. 15: Simplified illustration of the inferred boundaries of weathering zones within a saprolite mantle; based on spot measurements from two sections and interpretation of the resulting pore-throat-size distribution curves; note that boundaries of weathering zones are irregular in outline and are not parallel to the ground surface.

Pore-throat size data from saprolite specimens can be used to aid in the interpretation of tracer behavior. McKay et al. (1995) performed microbial tracer experiments within the saprolite mantle (developed from Nolichucky Shale) of Bear Creek Valley on the ORR. Colloidal tracers for the experiments included bacteriophages PRD-1 (diameter of 62 nm) and MS-2 (diameter 26 nm), INA (a dead bacteria strain with an average diameter of 1000 nm), and also fluorescent polymer microspheres (diameter of 100 nm). The faster migration of the colloid-sized tracers, when compared to non-reactive solute tracers (He, Ne; Sanford and Solomon, 1995), is attributed to diffusion of the solute tracers into the saprolite-matrix pore space but not of the larger sized colloidal tracers (McKay et al., 1995). McKay et al. (1995) interpret the large loss of colloids with distance from the injection well to be the result of filtration and sorption. The fast transport of colloid-sized tracers is accomplished within the interconnected fracture network of the saprolite mantle. The effective porosity provided by this fracture network was not determined but is believed to be relatively small, compared to the effective porosity of the saprolite matrix (Sanford, pers. comm.).

Figure 16 shows the pore-throat size distributions of the analyzed saprolite-groundmass specimens (see Appendix III). Groundmass is volumetrically the by far dominant part of the saprolite matrix. Superimposed on the curves are the sizes of colloidal-sized tracers. It is apparent that the pore-throat sizes are large and abundant enough to allow access of colloidal tracers into the saprolite-matrix pore space. Matrix diffusion is absent or minimal for colloidal tracers not because of size exclusion (especially for PRD-1 and MS-2), but probably because of relatively small diffusion coefficients. The reduction in concentration of colloidal tracers might be explained by infiltration of colloidal tracers into the saprolite-matrix pore space through active flow, either from the injection borehole into the wall of the borehole or from fractures into fracture walls. The smaller sized colloidal tracers (PRD-1 and MS-2) have more of the pore space available for infiltration (Figure 16) and will show a more severe reduction in concentration, as reported by McKay et al. (1995).

Fig. 16: Pore-throat-size distribution curves of saprolite groundmass specimens with superimposed sizes of colloidal tracers. The tracers (and their diameter) are as follows: 1 - MS-2 (26 nm), 2 - PRD-1 (62 nm), 3 - polymer microspheres (100 nm), 4 - INA (average of 1000 nm). For deeper intervals of the saprolite mantle, saprolite-groundmass specimen GW-823-5 probably provides the best approximation of throat sizes and their distribution. All documented pore-throat sizes fall within the micropore category for soils, as proposed by Luxmoore (1981).

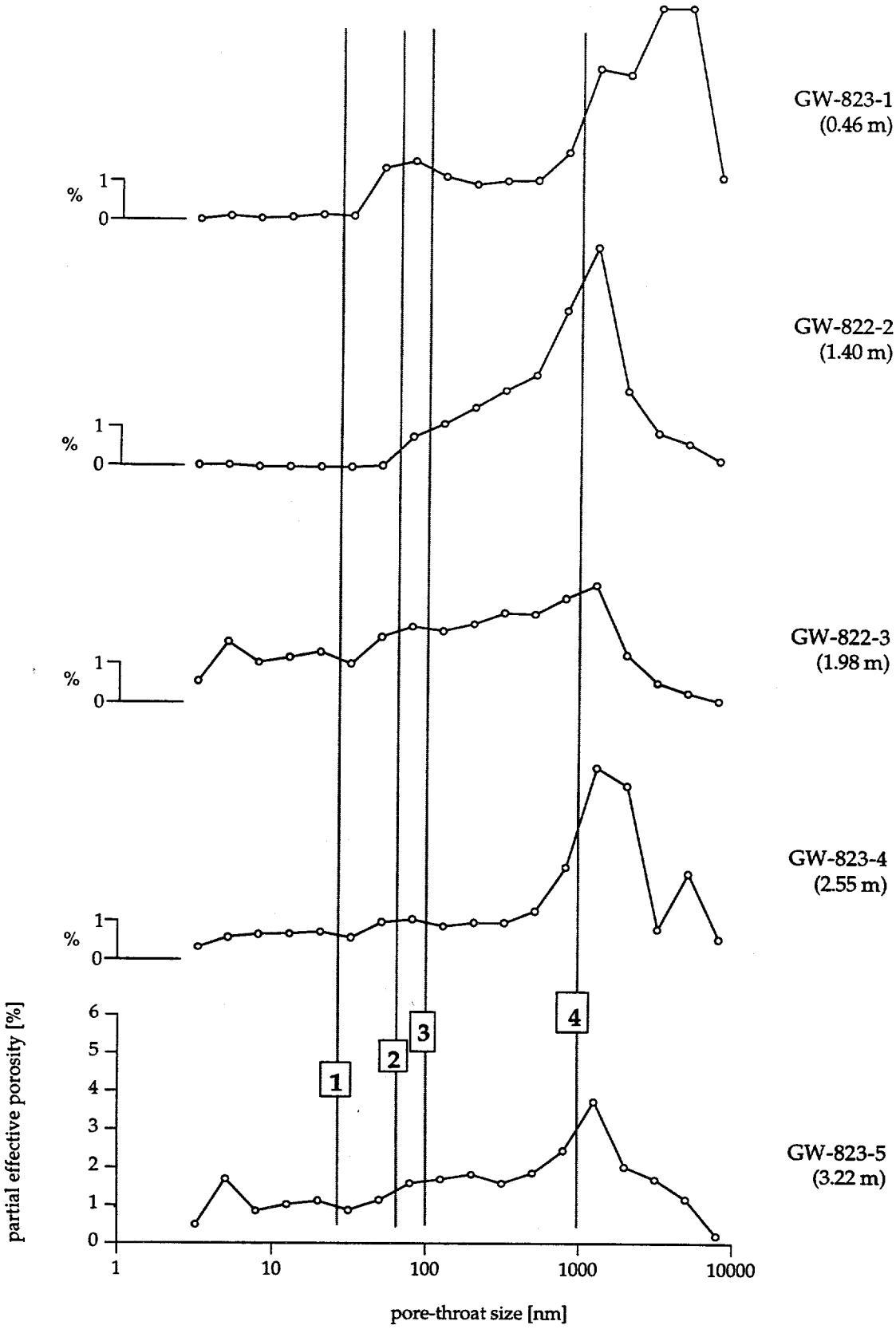
GW-823-1
(0.46 m)
GW-822-2
(1.40 m)
GW-822-3
(1.98 m)
GW-823-4
(2.55 m)
GW-823-5
(3.22 m)
%
1
0
1
2
3
4
partial effective porosity [%]
pore-throat size [nm]
1
10
100
1000
10000

Effective Porosity Data

Comparison of Effective Porosities. Effective porosity values of saprolite specimens based on helium porosimetry are higher than effective porosity values based on mercury porosimetry (Table 2; Figure 17). This observation is in accordance with earlier studies on bedrock mudrock from different sedimentary basins (Issler and Katsube, 1994; Dorsch et al., 1996). The lone exception is the Hg-2 data for saprolite-groundmass specimen GW-823-5 (Table 2; Figure 17).

A characteristic of all pore-throat-size distribution curves of analyzed saprolite specimens (except GW-823-1) is their abrupt termination at a pore-throat size of about 3 nm (Appendix IV). This corresponds to the analytical limit of commonly available mercury porosimeters, which cannot produce intrusion pressures high enough to force mercury into pores accessed by pore throats ≤3 nm. The discrepancy between helium effective porosities and mercury effective porosities most likely reflects that the analyzed specimens possess pore space sheltered by pore throats ≤3 nm in size, precluding characterization by mercury but still allowing access by helium (Katsube, 1992; Issler and Katsube, 1994). This is in accordance with observations and interpretations on mudrock specimens from the Conasauga Group (bedrock) on the ORR (Dorsch et al., 1996). Based on this interpretation, the helium effective porosity data should be considered as a true reflection of the (maximum) effective porosity of the analyzed saprolite specimens.

Saprolite-groundmass data show also a truncation at about 8000 nm in the pore-throat-size distribution curves (based on Hg1-data; Appendix IV). This might provide the opportunity for pore space sheltered by pore throats larger than about 8000 nm in size (not reported in the mercury data) which might add to the difference between helium and mercury effective porosities.

The large differences in helium and mercury effective porosities for saprolite-groundmass specimens GW-822-2 and GW-823-1 deserve special consideration. Pore-throat-size distribution curves (Appendix IV) show zero or very low values for pore-throat sizes from about 30 to about 5 nm for GW-822-2 (and less pronounced for GW-823-1). Then it appears that pore-throat sizes smaller than about 5 nm again are present. This observation might reflect the possibility of a secondary creation of pore throats ≤5 nm in size through progressive chemical weathering. The increase in the difference between helium and mercury effective porosities in the most weathered zones might be explained by these added pore throats ≤5 nm (and especially ≤3 nm) in size and their difference in accessibility to mercury and helium.

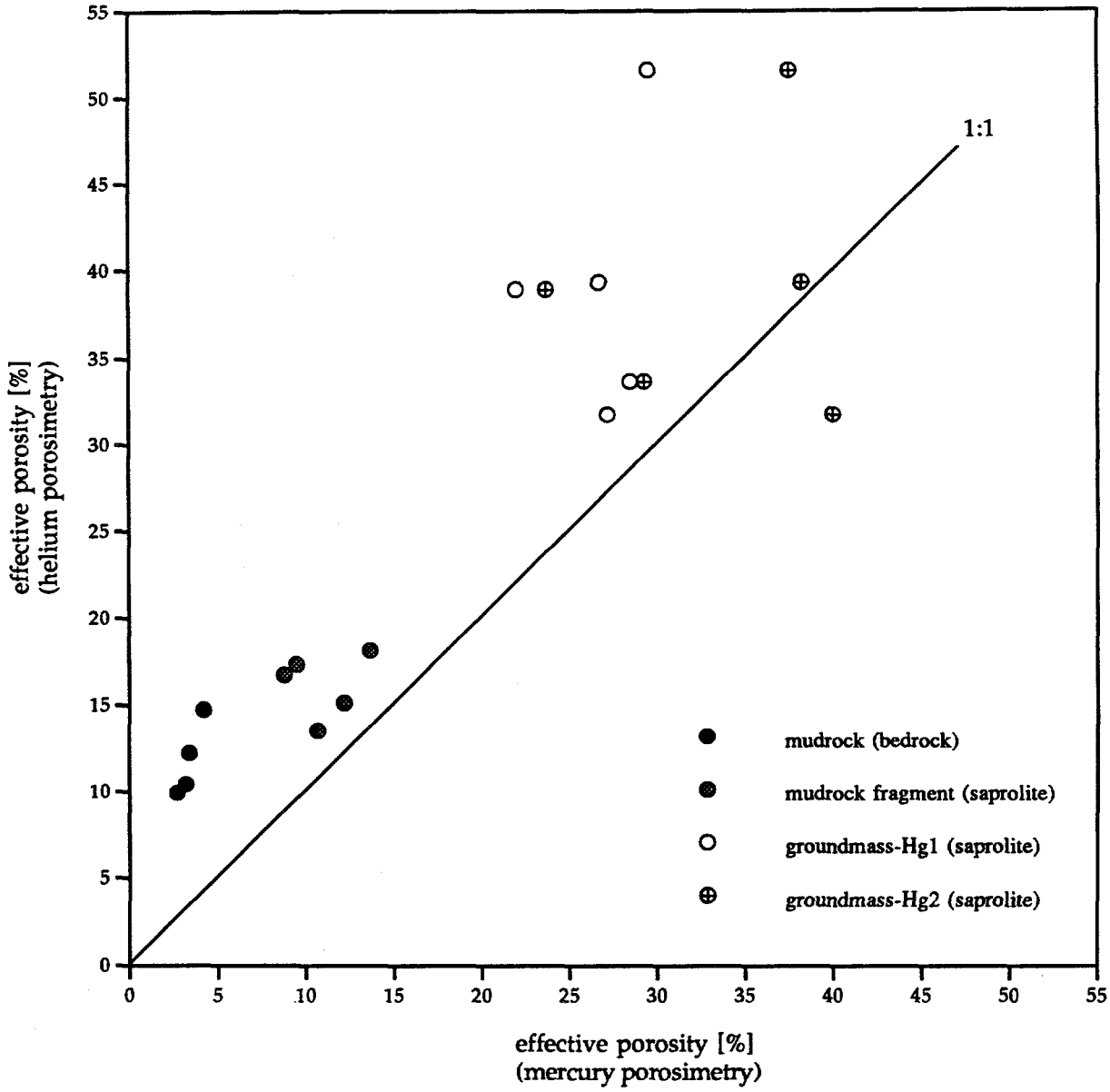

Fig. 17: Diagram plotting effective porosity based on mercury porosimetry against effective porosity based on helium porosimetry. Specimens are from Nolichucky Shale (bedrock) and from saprolite (mudrock fragments and groundmass), Bear Creek Valley on the ORR. Hg1-data are plotted throughout, and in addition Hg2-data for saprolite-groundmass specimens. Bedrock specimens with anomalously low effective porosity values based on helium porosimetry (see Dorsch et al., 1996) were disregarded.

A remaining problem is saprolite-groundmass specimen GW-823-5 whose Hg2-effective porosity exceeds helium effective porosity (Table 2). Reexamination of partial porosity data above pore-throat size 10000 nm showed a large amount of mercury intrusion at a size of 13000 nm. This most likely reflects a microcrack of diameter 13000 nm, which was not present in the groundmass specimen from the same sampling interval analyzed with helium porosimetry. (It is important to reiterate, that specimens with *visible* cracks were not used in analyses.) Specimen GW-823-5 was the only example showing this effective porosity signature. This can be interpreted to indicate that the other groundmass specimens were probably devoid of microcracks of a size >8000 nm. The occurrence of the microcrack might reflect heterogeneity on that scale within the sampling interval or might indicate an origin during the drying process for this single specimen.

The scatter for saprolite mudrock-fragments is small for helium and mercury effective porosities, whereas for saprolite-groundmass specimens the scatter is larger. This corresponds to observations on specimen density data and is interpreted to indicate the increased effect of weathering on saprolite-groundmass specimens.

Comparison to Bedrock. Mudrock specimens from the Nolichucky Shale (bedrock) show a mean effective porosity of 11.8 (±2.2)% based on helium porosimetry with a minimum and maximum value of 9.9% and 14.7% (Appendices II, VI) (note: only reliable helium-porosimetry data were used, n = 4; see discussion in Dorsch et al., 1996). Mercury-porosimetry data, in contrast, are much lower with a mean of 3.9 (±0.7)% and a range from 2.7% to 5.1% (Appendices II, VI).

Helium-porosimetry data for saprolite mudrock-fragments are slightly higher than for bedrock mudrock, with their scatter being virtually identical (Figure 18). There is a distinct increase in value and scatter, however, for saprolite-groundmass specimens. Mercury-porosimetry data separate into distinct groups, with a step-wise increase in effective porosity from bedrock mudrock, through saprolite mudrock-fragments, to saprolite-groundmass specimens (Figure 18).

The increase in effective porosity and in scatter from bedrock mudrock to saprolite groundmass is again interpreted to reflect the increasing degree of changes associated with weathering. Dissolution of pore- and pore-throat-lining cement (predominantly carbonate) during chemical weathering enlarged pores and pore throats and can explain the increase in effective porosity from bedrock to saprolite mudrock fragments. Even more intense weathering and further dissolution of cement and of grain material, together with mechanical loosening of the grain fabric, may have caused the

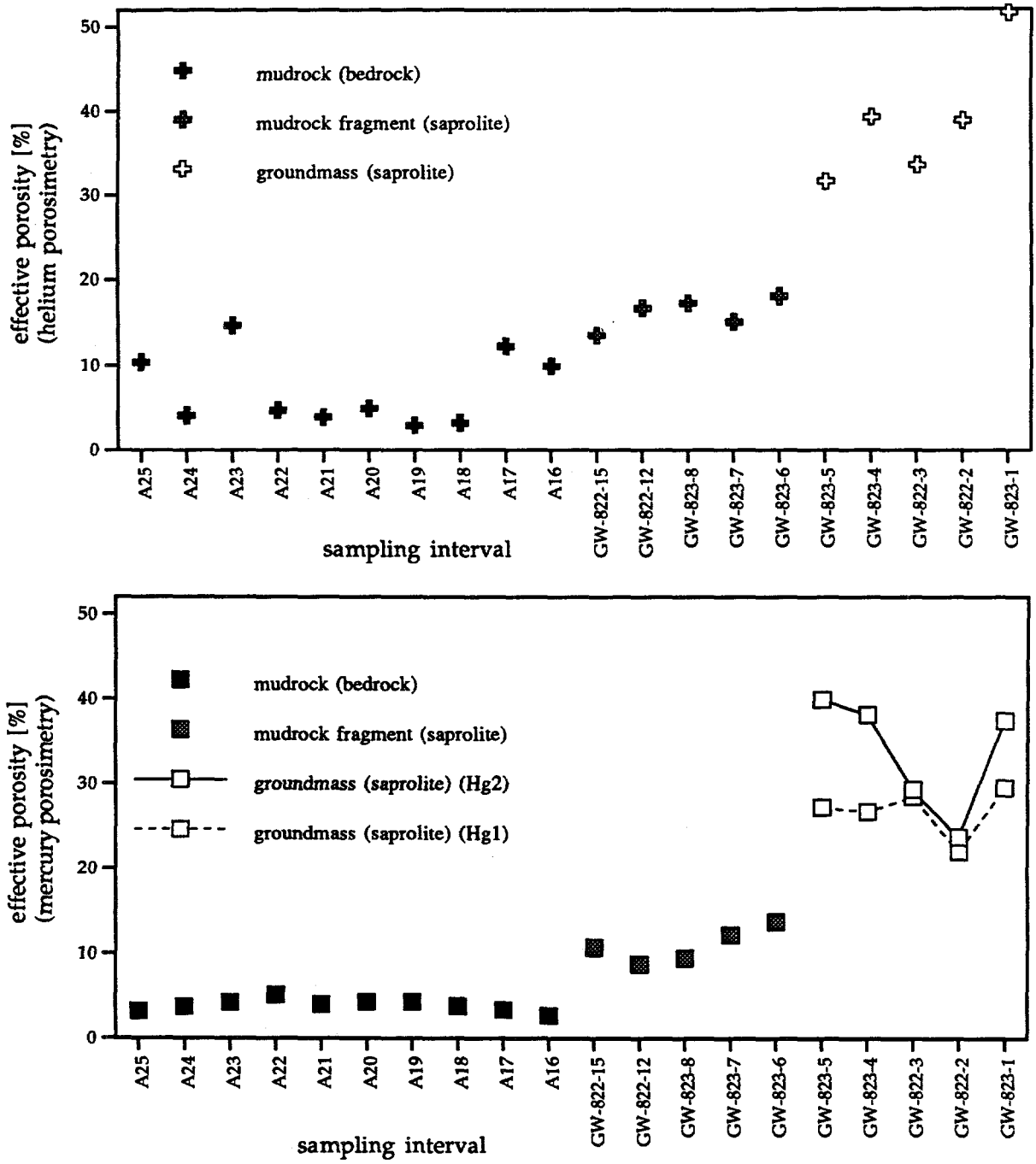

Fig. 18: Comparison of helium-porosimetry (upper graph) and mercury-porosimetry (lower graph) effective porosity data obtained from Nolichucky Shale (bedrock) and saprolite (mudrock fragments and groundmass), Bear Creek Valley on the ORR.

drastic increase in effective porosity and scatter for saprolite groundmass.

The larger difference between effective porosity based on helium porosimetry and on mercury porosimetry for bedrock mudrock compared to saprolite mudrock-fragments might reflect that a larger part of the interconnected pore space in bedrock mudrock is sheltered by access pore-throats ≤3 nm in size (Dorsch et al., 1996). Weathering reduced the fraction of pore throats ≤3 nm for saprolite mudrock-fragments and mercury was able to characterize a larger fraction of the interconnected pore space. Helium, on the other hand, is not inhibited from accessing pore throats ≤3 nm in size (Katsube, 1992; Issler and Katsube, 1994).

Effective Porosities with Depth. A trend toward increasing effective porosity with decrease in depth is clearly discernible from the tightly clustered helium-porosimetry (only reliable data from bedrock) and mercury-porosimetry data when progressing from bedrock into the saprolite zone (Figure 19). This trend continues from saprolite mudrock-fragments to saprolite-groundmass specimens. The more drastic "jump" toward higher effective porosity values from saprolite mudrock-fragments to saprolite groundmass is caused by comparing mudrock fragments to groundmass. Saprolite groundmass occurs also at depths from which saprolite mudrock-fragments were collected (and vice versa), although in a smaller proportion. A comparison of groundmass (or mudrock fragments) throughout the saprolite mantle is expected to yield the same trend of increasing effective porosity with decreasing depth, albeit this trend is presumed to be smoother with a less severe "jump" in effective porosity values. The same statement applies for the drastic "jump" in bulk-density values within the saprolite mantle (Figure 13).

The effective porosity trend with depth reflects the decrease in weathering and associated changes with depth. The general depth profile is more complicated when the data within the two saprolite specimen groups (mudrock fragments and groundmass) are compared. Mercury-porosimetry data for saprolite mudrock-fragments conforms to the weathering picture developed from the analysis of pore-throat-size distribution curves (Figure 15), whereas helium-porosimetry data do not. Anomalously high helium-porosimetry data for GW-822-12 and GW-823-8, however, fall within the uncertainty of the analysis method. Helium-porosimetry data for saprolite groundmass correspond exactly to the weathering picture developed from the analysis of pore-throat-size distribution curves (Figure 15), as do most of the mercury-porosimetry data. Exceptions are specimens GW-823-5 (Hg2-data, explained above) and GW-822-2 (Hg1- and Hg2-

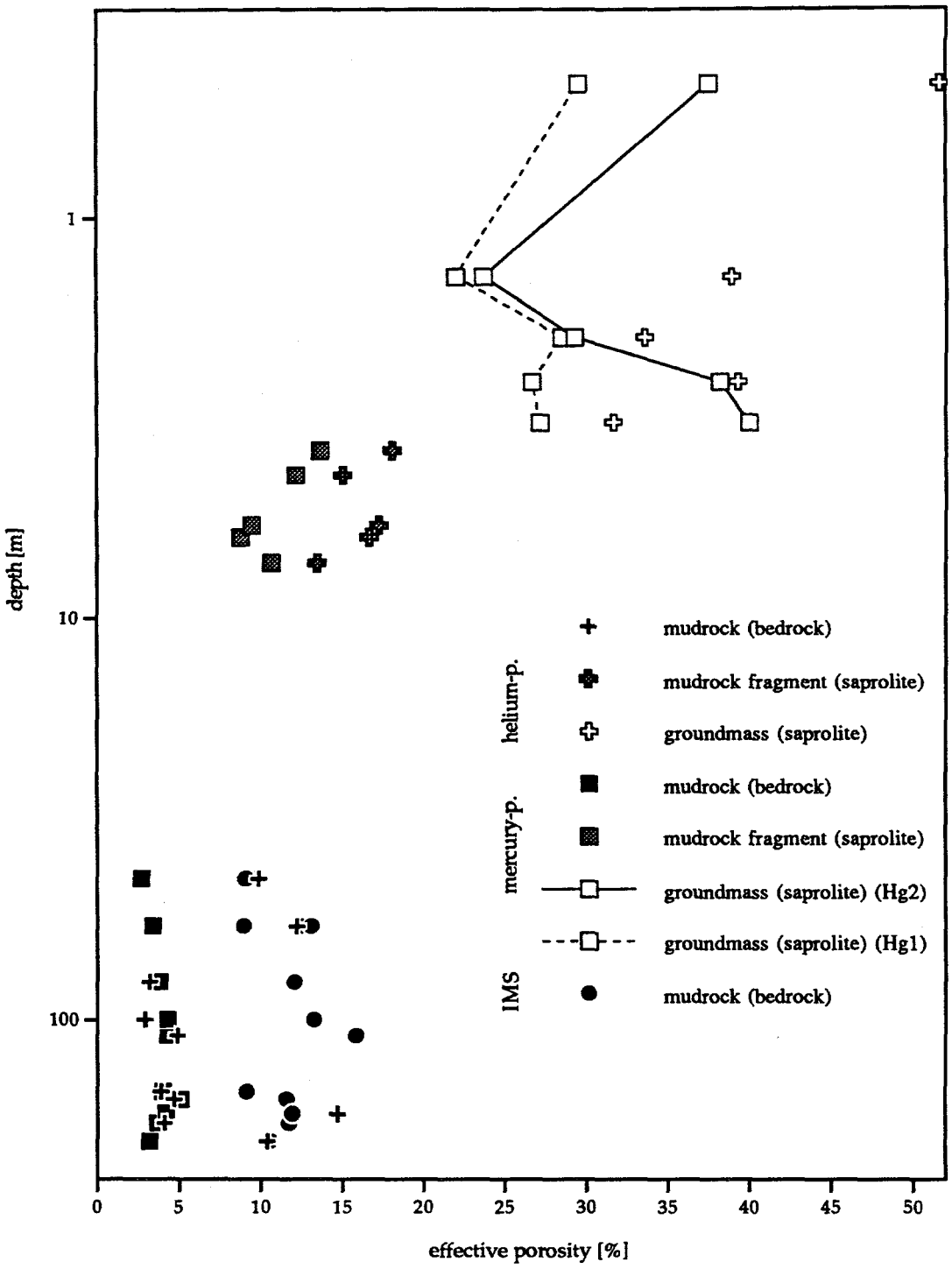

Fig. 19: Effective porosity with depth for Nolichucky Shale and saprolite specimens, Bear Creek Valley on the ORR. Maximum depth is 201.19 m, minimum depth is 0.46 m; depth is given as below ground surface. IMS refers to effective porosity obtained with the water-immersion method, mercury-p. and helium-p. refer to effective porosity obtained with mercury and helium porosimetry, respectively (note log-scale on depth axis).

data are too low). The anomalously low mercury-porosimetry values (compared to the corresponding helium-porosimetry value) for specimen GW-822-2 probably emphasize newly created pore throats ≤5 nm in size caused by continued weathering (Appendices III, IV; see discussion above). Pore throats of this size shelter larger pores which cannot be accessed by mercury (lower detection limit of about 3 nm) but by helium.

Overall, however, the effective porosity data within the different saprolite-specimen groups support the notion of irregularly-shaped boundaries of weathering zones within the saprolite mantle as developed previously from the analysis of pore-throat-size distribution curves (Figure 15).

Calculated interval effective porosities show an exponential decrease in effective porosity with depth (Figure 20). This is interpreted to clearly show the increasing effect weathering had on the rock material with decreasing depth. Note the smooth transition toward lower effective porosity values with depth within the saprolite mantle. The prominent jump in petrophysical data within the saprolite mantle, observed in Figures 13 and 18, is missing. A distinct jump toward lower effective porosity values (matrix), however, will occur at the saprolite-bedrock interface (compare to Lietzke et al., 1988), with average mudrock (bedrock) effective porosities (helium) of 11.8% (maximum 14.7%) (Appendix 2; Figure 20) vs. 26.2% as the lowest saprolite-matrix effective porosity value.

The calculated saprolite matrix effective porosities conform to the picture of weathering zones and their boundaries (Figure 15), although the differences are more subtle (especially below 5 m depth).

The interval effective porosities are judged to be meaningful, especially for the modeling of contaminant behavior. They constitute quantitative data on saprolite-matrix effective porosities over a larger saprolite volume, instead of effective porosities for small-volume specimens as used for petrophysical analysis. Furthermore, interval effective porosities incorporate the contribution of both types of saprolite materials, groundmass and "floating" mudrock fragments. The largest degree of uncertainty with these calculated effective porosity data is probably provided by the visual estimation of the proportion of groundmass vs. mudrock fragments for the chosen saprolite intervals.

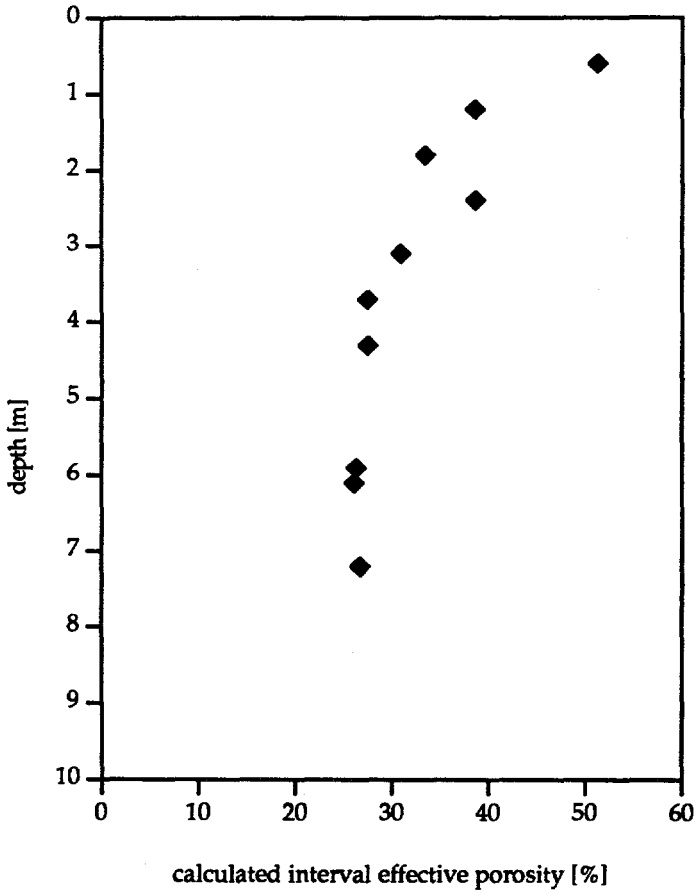

Fig. 20: Calculated interval effective porosity against depth. Porosities are based on helium porosimetry; for calculation and data see Appendix V. Depths are medians of intervals and are given as below ground surface.

CONCLUSIONS

1. Specimens of mudrock saprolite from Bear Creek Valley, developed from Nolichucky Shale through weathering, were analyzed with helium and mercury porosimetry (Table 3). The undisturbed and fresh cores of the saprolite mantle yield two types of specimens: the volumetrically dominating, more extensively weathered saprolite groundmass and saprolite mudrock-fragments contained within the saprolite groundmass.

2. Saprolite mudrock-fragments possess average bulk-densities of 2.44 $g \cdot cm^{-3}$, and average grain-densities of 2.80 $g \cdot cm^{-3}$. Helium effective porosities are 16.1% and mercury effective porosities are 11.9% on average.

3. Saprolite-groundmass specimens possess average bulk-densities of 1.79 $g \cdot cm^{-3}$ and average grain-densities of 2.79 $g \cdot cm^{-3}$. Helium effective porosities are 39.0% and mercury effective porosities are 33.7% (Hg2) or 26.8% (Hg1) on average.

4. Effective porosity values from helium porosimetry are generally higher than values from mercury porosimetry for the same sampling interval. Mercury effective porosities are lower because of mechanical limitations of the analytical equipment. Helium effective porosities, therefore, are considered to provide the best estimates of the true (maximum) effective porosity of the analyzed specimens.

5. Petrophysical data display a consistent trend from bedrock mudrock, to saprolite mudrock-fragments, to saprolite groundmass: effective porosities (both helium and mercury) increase and specimen bulk-densities decrease, together with an increase in scatter of the data. This is interpreted to reflect the progressive effect of weathering on the rock material. Cement and some grain material was probably lost during weathering together with a gradual loosening of the grain fabric.

6. The pore-throat-size data for saprolite mudrock-fragments show normal distribution curves skewed toward the right with modes from 5 to 20 nm. Most of the pores are accessed by pore throats <100 nm in size. In marked contrast, pore-throat-size data for saprolite-groundmass specimens show normal distribution curves skewed toward the left with modes ranging from 1200 to 5000 nm. Most of the pores are accessed by pore throats >100 nm in size. The apparent shift of the throat-size spectrum toward larger sizes when progressing from bedrock mudrock, through saprolite mudrock-fragments, to saprolite groundmass reflects the progressive effect of weathering, with loss of pore-filling, pore-throat-lining and -plugging cement.

7. The pore-throat-size distribution curves also reveal that the boundaries of weathering zones are irregular in outline and do most likely not conform to the ground

Table 3: Summary of petrophysical information on saprolite specimens (groundmass and mudrock fragments) from Bear Creek Valley on the ORR. The saprolite developed from Nolichucky Shale of the Conasauga Group through weathering. Petrophysical data for Nolichucky Shale bedrock from Bear Creek Valley are provided in Appendix VI (compare also to Dorsch et al., 1996). ϕ refers to effective porosity determined with helium porosimetry (He) or mercury porosimetry (Hg1, Hg2, see text for discussion), whereas δ refers to specimen density (He = grain density, Hg = bulk density); d_{Hg} refers to the geometric mean of the entire specimen pore-throat size distribution.

Sampling Interval	Corehole	Depth [m]	ϕ_{He} [%]	ϕ_{Hg1} [%]	ϕ_{Hg2} [%]	d_{Hg} [nm]	δ_{He} [$g \cdot cm^{-3}$]	δ_{Hg} [$g \cdot cm^{-3}$]	Specimen Type (saprolite)
GW-823-1	GW-823	0.46	51.6	29.5	37.5	2201	2.76	1.48	groundmass
GW-822-2	GW-822	1.40	38.9	22.0	23.7	870	2.90	1.81	groundmass
GW-822-3	GW-822	1.98	33.6	28.5	29.3	182	2.87	1.92	groundmass
GW-823-4	GW-823	2.55	39.3	26.7	38.2	1823	2.70	1.64	groundmass
GW-823-5	GW-823	3.22	31.7	27.2	40.0	934	2.72	1.91	groundmass
GW-823-6	GW-823	3.79	18.1	13.7	14.0	27	2.78	2.36	mudr. fragment
GW-823-7	GW-823	4.37	15.1	12.2	12.8	24	2.78	2.39	mudr. fragment
GW-823-8	GW-823	5.84	17.3	9.5	10.1	25	2.80	2.40	mudr. fragment
GW-822-12	GW-822	6.25	16.7	8.8	9.2	18	2.81	2.50	mudr. fragment
GW-822-15	GW-822	7.24	13.5	10.7	11.2	28	2.81	2.53	mudr. fragment

surface. The data indicate, furthermore, the probable creation of an additional population of pore throats <5 nm in size for the most weathered specimens of saprolite groundmass, most likely caused by continued weathering.

8. Calculated interval effective porosities (based on petrophysical measurements and varied estimates) yield values between 51.3% and 26.2%. The values decrease exponentially with depth and mirror the decreasing influence of weathering on the rock material with depth. The calculated interval effective porosities incorporate larger volumes of saprolite matrix and integrate both groundmass and mudrock-fragment effective porosities of the chosen saprolite intervals. These data appear of special significance for modeling and evaluating matrix diffusion as a transport process within the saprolite mantle.

References

American Petroleum Institute (1960): *Recommended Practices for Core-analysis Procedure.* API Recommended Practice 40 (RP 40), 1st ed., American Petroleum Institute, Washington, D.C., 55 p.

Blatt, H., Middleton, G. V., and Murray, R. C. (1980): *Origin of Sedimentary Rocks.* Prentice-Hall, Englewood Cliffs, NJ, 782 p.

Dorsch, J. (1995): *Determination of effective porosity of mudrocks - A feasibility study.* ORNL/GWPO-019, 60 p.

Dorsch, J., Katsube, T. J., Sanford, W. E., Dugan, B. E., and Tourkow, L. (1996): *Effective porosity and pore-throat sizes of Conasauga Group Mudrock: Application, Test and Evaluation of Petrophysical Techniques.* ORNL/GWPO-021.

Dreier, R. B., Solomon, D. K., and Beaudoin, C. M. (1987): Fracture characterization in the unsaturated zone of a shallow land burial facility. In: *Flow and Transport through Fractured Rock.* American Geophysical Union Monograph 40, p. 51-59.

Dreier, R. B., Hatcher, R. D., Jr., Lietzke, D. A. (1992): 3.3 Conasauga Group. In: R. D. Hatcher, Jr., P. J. Lemiszki, R. B. Dreier, R. H. Ketelle, R. R. Lee, D. A. Lietzke, W. M. McMaster, J. L. Foreman, and S. Y. Lee: *Status Report on the Geology of the Oak Ridge Reservation.* ORNL/TM-12074, p. 18-41.

Fairbridge, R. W. (1968): Regolith and saprolite. In: R. W. Fairbridge, ed., *The Encyclopedia of Geomorphology,* p. 933-936.

Germain, D., and Frind, E. O. (1989): Modelling of contaminant migration in fracture networks: Effects of matrix diffusion. Proceedings International Symposium on Contaminant Transport in Groundwater, Stuttgart, Germany (April 1989), p.

Gwo, J. P., Jardine, P. M., Wilson, G. V., and Yeh, G. T. (1996): Using a multiregion model to study the effects of advective and diffusive mass transfer on local physical nonequilibrium and solute mobility in structured soil. Water Resources Research, v. 32, p. 561-570.

Hasson, K. O., and Haase, C. S. (1988): Lithofacies and paleogeography of the Conasauga Group (Middle and Late Cambrian) in the Valley and Ridge Province of East Tennessee. Geological Society of America Bulletin, v. 100, p. 234-246.

Hatcher, R. D., Jr., Lemiszki, P. J., Dreier, R. B., Ketelle, R. H., Lee, R. R., Lietzke, D. A., McMaster, W. M., Foreman, J. L., and Lee, S. Y. (1992): *Status Report on the Geology of the Oak Ridge Reservation.* ORNL/TM-12074, 247 p.

Issler, D. R., and Katsube, T. J. (1994): Effective porosity of shale samples from the Beaufort-Mackenzie Basin, northern Canada. In: *Current Research, Part B.* Geological Survey of Canada, p. 19-26.

Katsube, T. J. (1992): Statistical analysis of pore-size distribution data of tight shales from the Scotian Shelf. In: *Current Research, Part E.* Geological Survey of Canada, Paper 91-1E, p. 365-372.

Katsube, T. J., and Best, M. E. (1992): Pore structure of shales from the Beaufort-Mackenzie Basin, Northwest Territories. In: *Current Research, Part D.* Geological Survey of Canada, Paper 92-1E, p. 157-162.

Katsube, T. J., and Issler, D. R. (1993): Pore-size distributions of shales from the Beaufort-Mackenzie Basin, northern Canada. In: *Current Research, Part E.* Geological Survey of Canada, Paper-1E, p. 123-132.

Katsube, T. J., and Scromeda, N. (1991): Effective porosity measuring procedure for low porosity rocks. In: *Current Research, Part E.* Geological Survey of Canada, Paper 91-1E, p. 291-297.

Katsube, T. J., and Williamson, M. A. (1994): Shale petrophysics and basin charge modeling. In: *Current Research, Part D.* Geological Survey of Canada, Paper 91-1E, p. 291-297.

Katsube, T. J., Scromeda, N., and Williamson, M. (1992): Effective porosity from tight shales from the Venture gas field, offshore Nova Scotia. In: *Current Research, Part D.* Geological Survey of Canada, Paper 92-1D, p. 111-119.

Kopaska-Merkel, D. C. (1988): New applications in the study of porous media: Determination of pore-system characteristics on small fragments (part I). Northeastern Environmental Science, v. 7, p. 127-142.

Kopaska-Merkel, D. C. (1991): *Analytical Procedure and Experimental Design for Geological Analysis of Reservoir Heterogeneity using Mercury Porosimetry.* Alabama Geological Survey Circular 153, 29 p.

Lee, R. R., Ketelle, R. H., Bownds, J. M., and Rizk, T. A. (1992): Aquifer analysis and modeling in a fractured heterogeneous medium. Ground Water, v. 30, p. 589-597.

Lemiszki, P. J., and Hatcher, R. D., Jr. (1992): 5. Structure of the Oak Ridge Reservation. In: R. D. Hatcher, Jr., P. J. Lemiszki, R. B. Dreier, R. H. Ketelle, R. R. Lee, D. A. Lietzke, W. M. McMaster, J. L. Foreman, and S. Y. Lee: *Status Report on the Geology of the Oak Ridge Reservation.* ORNL/TM-12074, p. 109-178

Lietzke, D. A. (1992): 4. Oak Ridge Reservation soil survey. In: R. D. Hatcher, Jr., P. J. Lemiszki, R. B. Dreier, R. H. Ketelle, R. R. Lee, D. A. Lietzke, W. M. McMaster, J. L. Foreman, and S. Y. Lee: *Status Report on the Geology of the Oak Ridge Reservation.* ORNL/TM-12074, p. 69-107.

Lietzke, D. A., Lee, S. Y., and Lambert, R. E. (1988): *Soils, Surficial Geology, and Geomorphology of the Bear Creek Valley Low-Level Waste Disposal Development and Demonstration Program Site.* ORNL/TM-10573, 151 p.

Loman, J. M., Katsube, T. J., Correia, J. M., and Williamson, M. A. (1993): Effect of compaction on porosity and formation factor for tight shales from the Scotian Shelf, offshore Nova Scotia. In: *Current Research, Part E.* Geological Survey of Canada, Paper 93-1E, p. 331-335.

Luffel, D. L., and Howard, W. E. (1988): Reliability of laboratory measurement of porosity in tight gas sands. SPE Formation Evaluation, December, p. 705-710.

Luxmoore, R. J. (1981): Micro-, meso-, and macroporosity of soil. Soil Sci. Soc. Am. J., v. 45, p. 671-672.

McKay, L. D., Gillham, R. W., and Cherry, J. A. (1993): Field experiments in a fractured clay till 2. Solute and colloid transport. Water Resources Research, v. 29, p. 3879-3890.

McKay, L. D., Sanford, W. E., Strong-Gunderson, J., and De Enriquez, V. (1995): Microbial tracer experiments in a fractured weathered shale near Oak Ridge, Tennessee. Proceedings, Intern. Assoc. Hydrogeologists, Solutions '95 Conference. Edmonton, Alberta, Canada.

Moline, G. R., and Schreiber, M. E. (1995): *FY94 Site Characterization and Multilevel Well Installation at a West Bear Creek Valley Research Site on the Oak Ridge Reservation.* ORNL/TM-13029.

Neretnieks, I. (1980): Diffusion in the rock matrix: An important factor in radionuclide retardation? Journal of Geophysical Research, v. 85, p. 4379-4397.

Rootare, H. M. (1970): A review of mercury porosimetry. Perspectives of Powder Metallurgy, v. 5, p. 225-252.

Sanford, W. E., and Solomon, D. K. (1995): Noble gas solute tracer experiment in a fractured, weathered shale near Oak Ridge, Tennessee. Proceedings, Intern. Assoc. Hydrogeologists, Solutions '95 Conference. Edmonton, Alberta, Canada.

Sanford, W. E., Jardine, P. M., and Solomon, D. K. (1994): Examining matrix diffusion in fractured shales with noble gases. Geological Society of America Abstracts with Programs, v. 26, p. A362.

Schreiber, M. E. (1995): *Spatial Variability in Groundwater Chemistry in Fractured Rock: Nolichucky Shale, Oak Ridge, TN.* Unpublished M. Sc. thesis, University of Wisconsin, Madison, 248 p.

Scromeda, N., and Katsube, T. J. (1993): Effect of vacuum-drying and temperature on effective porosity determination for tight rocks. In: *Current Research, Part E.* Geological Survey of Canada, Paper-1E, p. 313-319.

Shevenell, L. M., Moore, G. K., and Dreier, R. B. (1994): Contaminant spread and flushing in fractured rocks near Oak Ridge, Tennessee. Ground Water Monitoring & Remediation, v. 14, p. 120-129.

Soeder, D. J. (1988): Porosity and permeability of eastern Devonian gas shales. SPE Formation Evaluation, v. 3, p. 116-138.

Solomon, D. K., Moore, G. K., Toran, L. E., Dreier, R. B., and McMaster, W. M. (1992): *Status Report: A Hydrologic Framework for the Oak Ridge Reservation.* ORNL/TM-12026. Oak Ridge National Laboratory, Oak Ridge, Tenn., variously paginated.

Tang, D. H., Frind, E. O., and Sudicky, E. A. (1981): Contaminant transport in fractured porous media: Analytical solution for a single fracture. Water Resources Research, v. 17, p. 555-564.

Toran, L., Sjoreen, A., and Morris, M. (1995): Sensitivity analysis of solute transport in fractured porous media. Geophysical Research Letter, v. 22, p. 1433-1436.

Wardlaw, N. C. (1976): Pore geometry of carbonate rocks as revealed by pore casts and capillary pressure. American Association of Petroleum Geologists Bulletin, v. 60, p. 245-257.

Wardlaw, N. C., McKellar, M., and Yu, Li (1988): Pore and throat size distribution determined by mercury porosimetry and by direct observation. Carbonates and Evaporites, v. 3, p. 1-15.

Washburn, E. W. (1921): Note on a method of determining the distribution of pore sizes in a porous material. Proceedings of the National Academy of Sciences, v. 5, p. 115-116.

Wickliff, D. S., Solomon, D. K., and Farrow, N. D. (1991): *Preliminary Investigation of Processes that affect Source Term Identification.* ORNL/ER 59, Oak Ridge National Laboratory, Oak Ridge, Tenn., 31 p.

APPENDIX I: Sampling Intervals

Summary information on sampling locations of specimens: designation of sampling intervals, cores, drill depths (below ground surface), and specimen type. 'Saprolite groundmass' and 'mudrock fragment' designate specimens from Nolichucky Shale saprolite, whereas 'mudrock (bedrock)' designates specimens from Nolichucky Shale bedrock within Bear Creek Valley.

Sampling Interval	Corehole	Drill Depth	Specimen Type
GW-822-2	GW-822	4' 7" (1.40 m)	saprolite groundmass
GW-822-3	GW-822	6' 6" (1.98 m)	saprolite groundmass
GW-823-1	GW-823	1' 6" (0.46 m)	saprolite groundmass
GW-823-4	GW-823	8' 4" (2.55 m)	saprolite groundmass
GW-823-5	GW-823	10' 7" (3.22 m)	saprolite groundmass
GW-822-12	GW-822	20' 6" (6.25 m)	mudrock fragment
GW-822-15	GW-822	23' 9" (7.24 m)	mudrock fragment
GW-823-6	GW-823	12' 5" (3.79 m)	mudrock fragment
GW-823-7	GW-823	14' 4" (4.37 m)	mudrock fragment
GW-823-8	GW-823	19' 2" (5.84 m)	mudrock fragment
A16	GW-134	145' 10" (44.45 m)	mudrock (bedrock)*
A17	GW-134	191' 2" (58.27 m)	mudrock (bedrock)*
A18	GW-134	263' 5" (80.29 m)	mudrock (bedrock)*
A19	GW-134	327' 5" (99.80 m)	mudrock (bedrock)*
A20	GW-134	359' 4" (109.53 m)	mudrock (bedrock)*
A21	GW-134	497' 4" (151.59 m)	mudrock (bedrock)*
A22	GW-134	519' 3" (158.27 m)	mudrock (bedrock)*
A23	GW-134	563' 10" (171.86 m)	mudrock (bedrock)*
A24	GW-134	617' 3" (181.14 m)	mudrock (bedrock)*
A25	GW-134	660' 1" (201.19 m)	mudrock (bedrock)*

* indicates specimens analyzed for an earlier study on Conasauga Group mudrock (Dorsch et al., 1996).

APPENDIX II: Statistical Measures

Some statistical measures calculated for specimens of Nolichucky Shale (bedrock) and saprolite (mudrock fragments and groundmass) from Bear Creek Valley on the ORR. Density measures are in $g \cdot cm^{-3}$ and porosity measures are in %. Abbreviations: x = arithmetic mean, sx = standard deviation, n = is number of specimen analyses, min = minimum value, max = maximum value. Data for bedrock specimens are from Dorsch et al. (1996). Note that helium-porosimetry measures for bedrock specimens lists only reliable values (see further detail in Dorsch et al., 1996).

	Specimen Type	x	sx	n	min	max
Specimen Grain-Density						
	mudrock (bedrock)	2.77	0.03	10	2.70	2.80
	mudrock fragment (saprolite)	2.80	0.02	5	2.78	2.81
	groundmass (saprolite)	2.79	0.09	5	2.70	2.90
Specimen Bulk-Density						
	mudrock (bedrock)	2.70	0.03	10	2.67	2.77
	mudrock fragment (saprolite)	2.44	0.07	5	2.36	2.53
	groundmass (saprolite)	1.75	0.19	5	1.48	1.91
Eff. Porosity Helium						
	mudrock (bedrock)	11.8	2.2	4	9.9	14.7
	mudrock fragment (saprolite)	16.1	1.8	5	13.5	18.1
	groundmass (saprolite)	39.0	7.8	5	31.7	51.6
Eff. Porosity Mercury						
	mudrock (bedrock)	3.9	0.7	10	2.7	5.1
	mudrock fragment (saprolite)	11.0	2.0	5	8.8	13.7
	groundmass (saprolite)	(26.8) 33.7	(2.9) 7.0	5	(22.0) 23.7	(29.5) 40.0

APPENDIX III: Results - Pore-Throat Sizes

Tabulation of pore-throat size data obtained with mercury porosimetry. Abbreviations are as follows: d (nm) refers to the geometric mean pore-throat sizes for the different pore-throat-size ranges (expressed in nanometers), ϕa refers to the partial porosity (expressed in percent), ϕ_{Hg1} refers to effective porosity measured by mercury porosimetry for pore-throat sizes ≤10 μm (expressed in percent), ϕ_{Hg2} refers to effective porosity measured by mercury porosimetry for pore-throat sizes ≤250 μm (expressed in percent), and dHg refers to the geometric mean of the entire pore-throat-size distribution (expressed in nanometers) for the analyzed specimen.

	GW-822-12	GW-822-15	GW-823-6	GW-823-7	GW-823-8	GW-822-2	GW-822-3	GW-823-1	GW-823-4	GW-823-5
d (nm)	ϕa [%]	ϕa [%]	ϕa [%]	ϕa [%]	ϕa [%]	ϕa [%]	ϕa [%]	ϕa [%]	ϕa [%]	ϕa [%]
3.2	0.85	0.53	0.45	0.79	0.67	0.04	0.61	0.00	0.38	0.50
5	1.95	1.54	1.27	1.77	1.99	0.05	1.65	0.09	0.64	1.70
7.9	1.32	1.04	1.39	1.87	1.63	0.00	1.11	0.03	0.72	0.86
12.6	1.27	1.72	1.96	2.08	1.46	0.00	1.25	0.06	0.74	1.03
20	1.00	1.79	2.64	2.15	1.27	0.00	1.40	0.13	0.79	1.13
31.6	0.65	1.04	1.65	0.86	0.60	0.00	1.09	0.10	0.65	0.88
50.1	0.75	1.36	2.10	1.17	0.65	0.04	1.80	1.36	1.05	1.15
79.4	0.50	0.73	1.13	0.55	0.53	0.80	2.07	1.55	1.13	1.59
126	0.25	0.35	0.45	0.31	0.22	1.14	1.96	1.14	0.95	1.70
200	0.15	0.23	0.21	0.17	0.14	1.57	2.15	0.95	1.05	1.83
316	0.07	0.18	0.12	0.12	0.12	2.01	2.45	1.04	1.05	1.59
501	0.05	0.05	0.07	0.07	0.02	2.42	2.42	1.06	1.36	1.87
794	0.02	0.05	0.14	0.12	0.00	4.09	2.84	1.80	2.51	2.46
1259	0.00	0.05	0.02	0.05	0.00	5.75	3.18	3.98	5.12	3.76
1995	0.00	0.00	0.02	0.05	0.00	2.01	1.36	3.82	4.65	2.04
3162	0.00	0.03	0.05	0.05	0.17	0.92	0.63	5.60	0.90	1.70
5012	0.00	0.00	0.02	0.00	0.00	0.65	0.38	5.60	2.36	1.18
7943	0.00	0.03	0.00	0.00	0.00	0.20	0.17	1.14	0.65	0.21
ϕ_{Hg1} [%]	8.8	10.7	13.7	12.2	9.5	22.0	28.5	29.5	26.7	27.2
ϕ_{Hg2} [%]	9.2	11.2	14.0	12.8	10.1	23.7	29.3	37.5	38.2	40.4
d_{Hg} [nm]	18	28	27	24	25	870	182	2201	1823	934

APPENDIX IV: Pore-Throat-Size Distribution-Curves

Pore-throat-size distribution curves for Nolichucky Shale saprolite specimens from Bear Creek Valley on the ORR analyzed with mercury porosimetry.

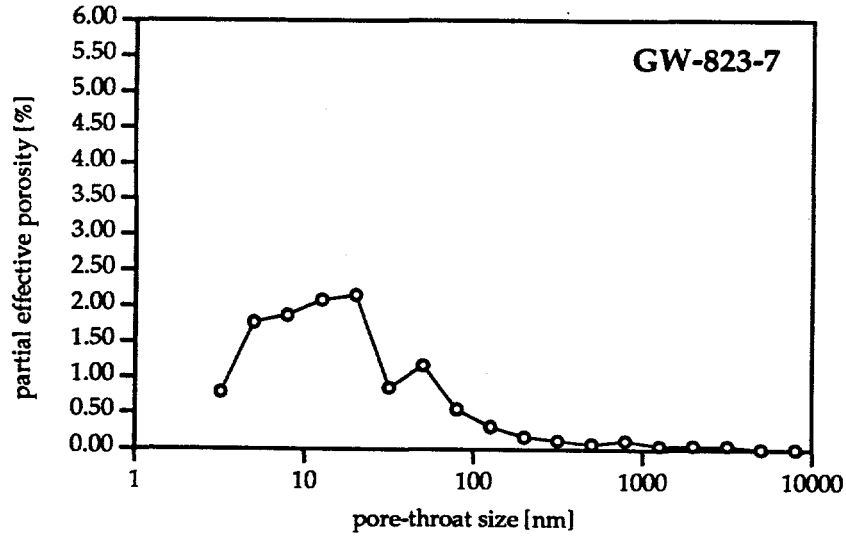

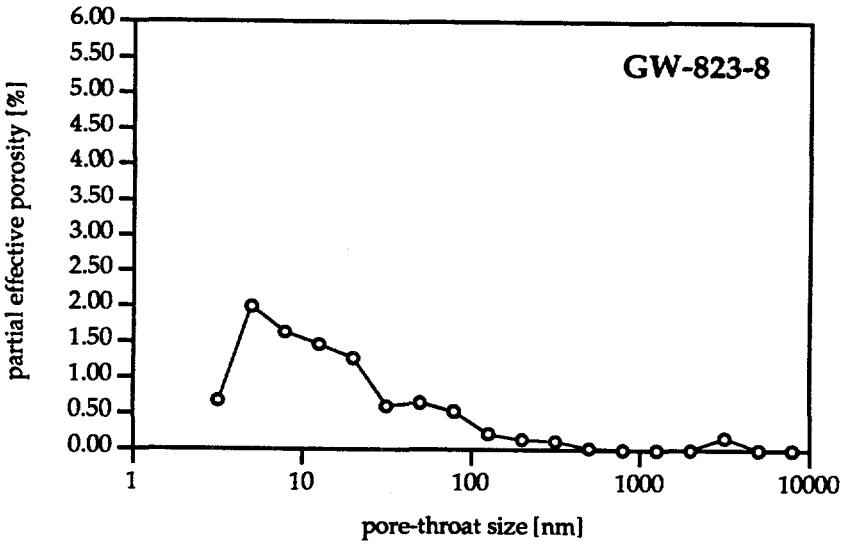

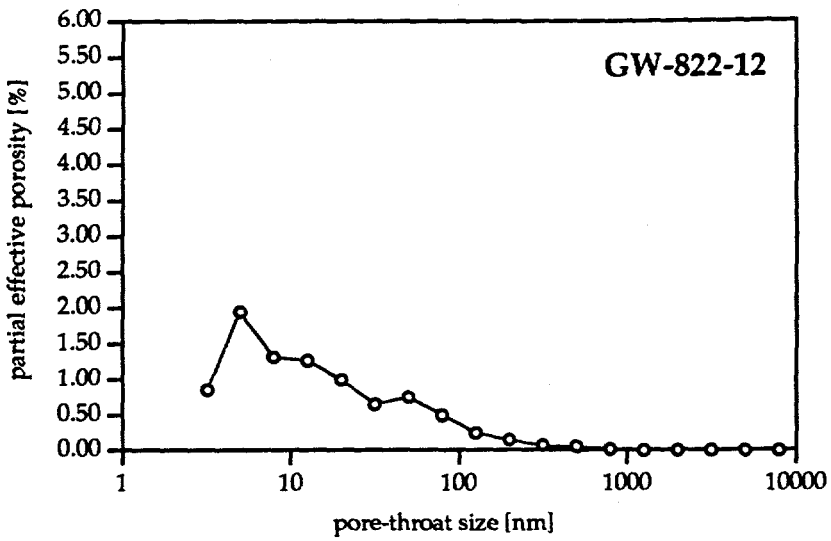
GW-822-12
partial effective porosity [%]
6.00
5.50
5.00
4.50
4.00
3.50
3.00
2.50
2.00
1.50
1.00
0.50
0.00
1
10
100
1000
10000
pore-throat size [nm]

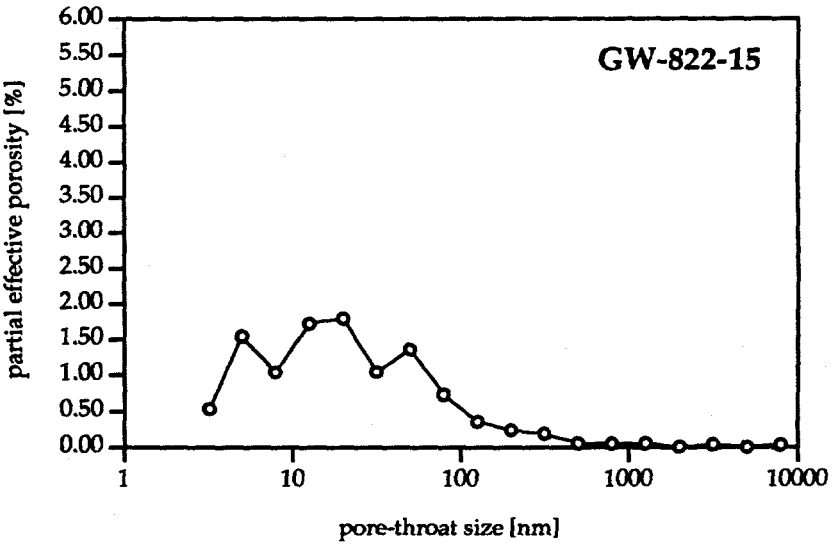
GW-822-15
partial effective porosity [%]
6.00
5.50
5.00
4.50
4.00
3.50
3.00
2.50
2.00
1.50
1.00
0.50
0.00
1
10
100
1000
10000
pore-throat size [nm]

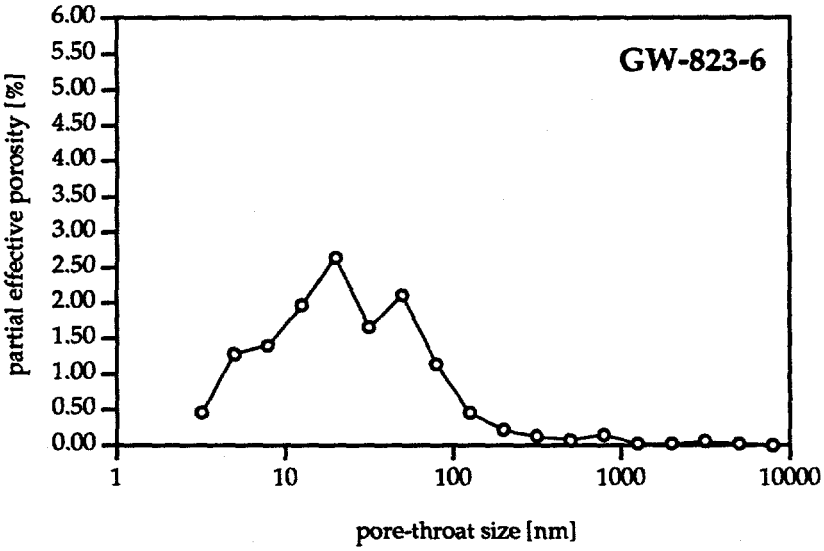
GW-823-6
partial effective porosity [%]
6.00
5.50
5.00
4.50
4.00
3.50
3.00
2.50
2.00
1.50
1.00
0.50
0.00
1
10
100
1000
10000
pore-throat size [nm]

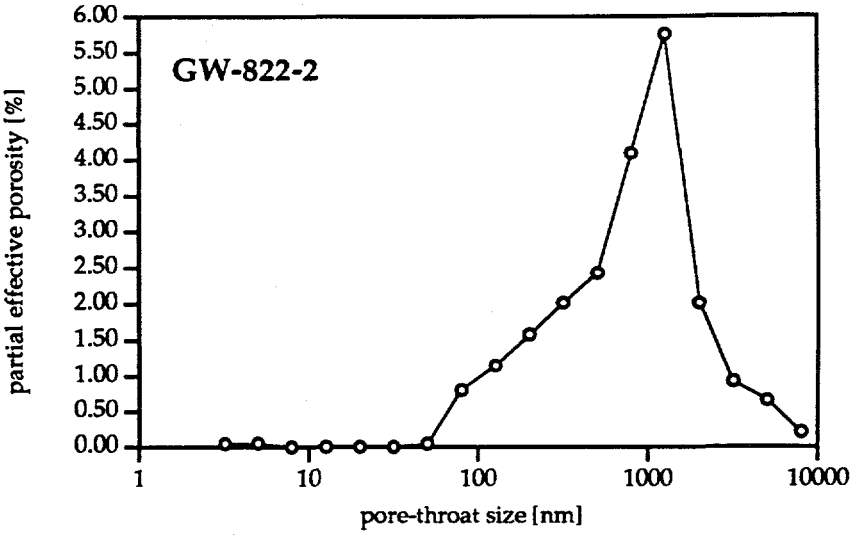
GW-822-2
partial effective porosity [%]
6.00
5.50
5.00
4.50
4.00
3.50
3.00
2.50
2.00
1.50
1.00
0.50
0.00
1
10
100
1000
10000
pore-throat size [nm]

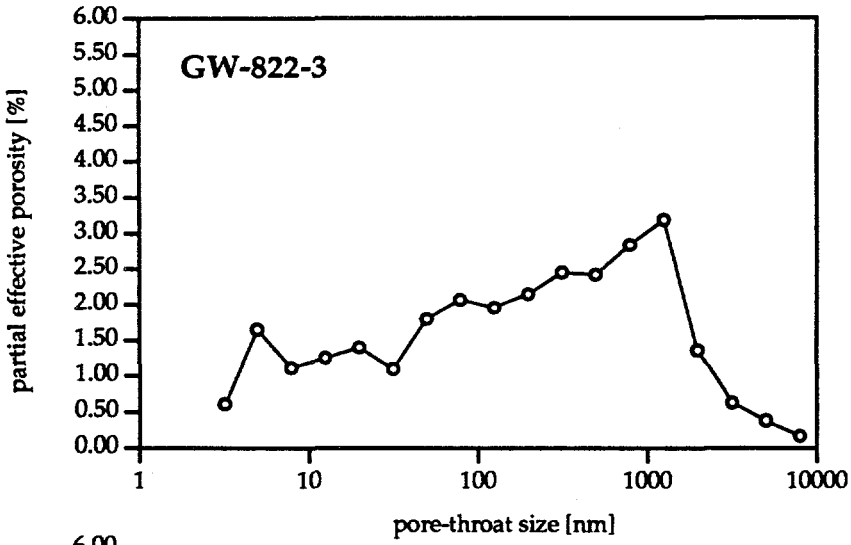
GW-822-3
partial effective porosity [%]
6.00
5.50
5.00
4.50
4.00
3.50
3.00
2.50
2.00
1.50
1.00
0.50
0.00
1
10
100
1000
10000
pore-throat size [nm]

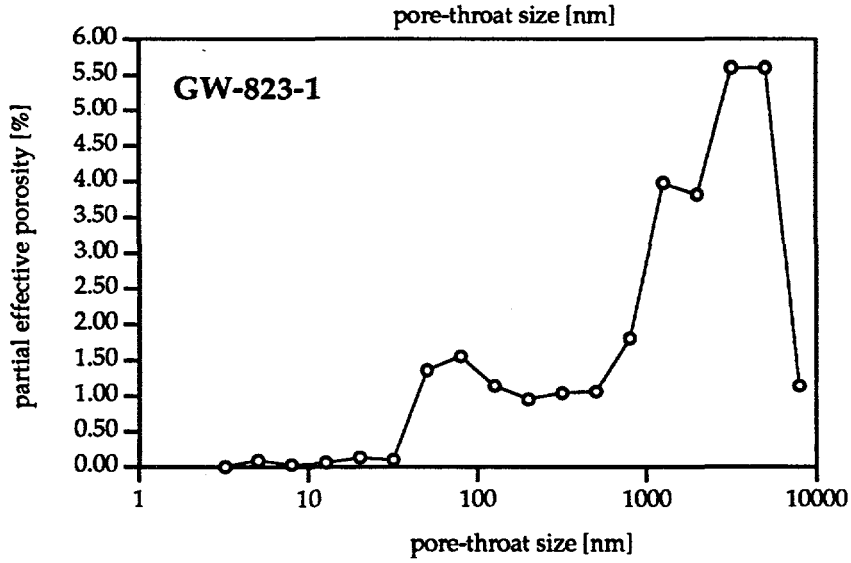
GW-823-1
partial effective porosity [%]
6.00
5.50
5.00
4.50
4.00
3.50
3.00
2.50
2.00
1.50
1.00
0.50
0.00
1
10
100
1000
10000
pore-throat size [nm]

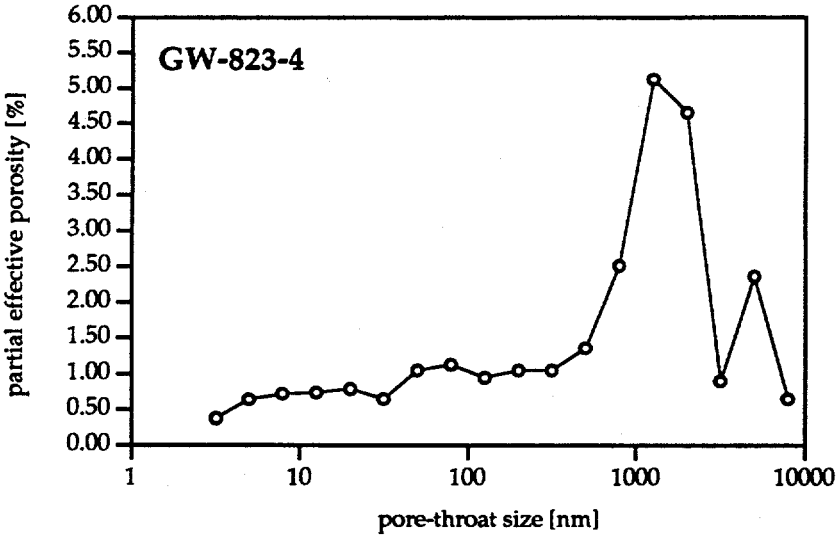
GW-823-4
partial effective porosity [%]
6.00
5.50
5.00
4.50
4.00
3.50
3.00
2.50
2.00
1.50
1.00
0.50
0.00
1
10
100
1000
10000
pore-throat size [nm]

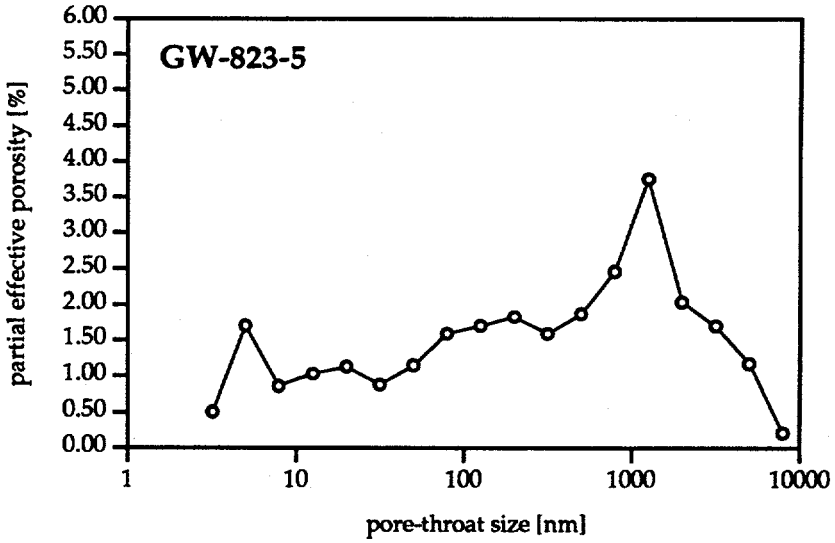
GW-823-5
partial effective porosity [%]
6.00
5.50
5.00
4.50
4.00
3.50
3.00
2.50
2.00
1.50
1.00
0.50
0.00
1
10
100
1000
10000
pore-throat size [nm]

APPENDIX V: Data for Calculation of Interval Effective Porosity

Summary of data used for the calculation of interval effective porosity of saprolite developed from Nolichucky Shale, Bear Creek Valley on the ORR. Depth range is given as below ground surface. Effective porosity data were determined with helium porosimetry, judged to more likely provide accurate (maximum) effective porosity values. Assumed effective porosity values are to complement measured effective porosity values for the different sampling intervals. The assumed value for mudrock fragments is the highest effective porosity value from a mudrock fragment below interval 5. It is judged as the most weathered petrophysically tested mudrock fragment and is interpreted to best approximate the effective porosity of mudrock fragments within intervals 1 to 5. The assumed value for groundmass is the lowest effective porosity value from a groundmass specimen above interval 6. It is judged as the least weathered petrophysically tested groundmass specimen and is interpreted to best approximate the effective porosity of saprolite groundmass within intervals 6 to 15. For intervals 1 through 5, the assumed value (for mudrock fragment) probably is a minimum value which makes the calculated interval effective porosities also minimum values (note, however, that these intervals are strongly dominated by groundmass, reducing severely the impact of mudrock fragment effective porosity). For intervals 6 through 15, the assumed value (for groundmass) probably is a maximum value which makes the calculated interval effective porosities also maximum values. The largest degree of uncertainty is provided by visually estimating the proportion of groundmass vs. mudrock fragments within the chosen saprolite intervals. Intervals 6 through 15 have a higher degree of uncertainty, with interval 15 providing the most difficulty for estimation.

interval	corehole	depth range (below ground surf.)	proportion fragments	proportion groundmass	specimen eff. porosity [%] fragments	specimen eff. porosity [%] groundmass	calculated interval eff. porosity [%]
1	GW-823	0.3 m to 0.9 m	0.01	0.99	18.1*	51.6	51.3
2	GW-822	0.9 m to 1.5 m	0.01	0.99	18.1*	38.9	38.7
3	GW-822	1.5 m to 2.1 m	0.01	0.99	18.1*	33.6	33.5
4	GW-823	2.1 m to 2.7 m	0.03	0.97	18.1*	39.3	38.7
5	GW-823	2.7 m to 3.4 m	0.05	0.95	18.1*	31.7	31.0
6	GW-823	3.4 m to 4.0 m	0.30	0.70	18.1	31.7*	27.6
7	GW-823	4.0 m to 4.6 m	0.25	0.75	15.1	31.7*	27.6
8	GW-823	5.6 m to 6.1 m	0.37	0.63	17.3	31.7*	26.4
12	GW-822	5.8 m to 6.4 m	0.37	0.63	16.7	31.7*	26.2
15	GW-822	7.0 m to 7.3 m	0.27	0.73	13.5	31.7*	26.8

* assumed effective porosity values

APPENDIX VI: Nolichucky Shale Petrophysical Data

Summary of petrophysical data for Nolichucky Shale specimens (bedrock) from Bear Creek Valley on the ORR. Data are from Dorsch et al. (1996) who also provide additional detail. Abbreviations: δ_{He} = specimen grain-density, δ_{Hg} = specimen bulk-density, d_{Hg} = geometric mean of the entire pore-throat-size distribution for the analyzed specimen, ϕ_{He} = effective porosity based on helium porosimetry, ϕ_{Hg} = effective porosity based on mercury porosimetry, and ϕ_{IMS} = effective porosity based on the immersion-saturation method. Drill depths are given in meters below ground surface. All data are from specimens obtained from corehole GW-134.

Sampling Interval	Drill Depth [m]	δ_{He} [g·cm^{-3}]	δ_{Hg} [g·cm^{-3}]	d_{Hg} [nm]	ϕ_{He} [%]	ϕ_{Hg} [%]	ϕ_{IMS} [%]
A16	44.45	2.73	2.69	31.9	9.9	2.7	9.46*
A17	58.27	2.78	2.70	51.2	12.2	3.4	11.52*
A18	80.29	2.79	2.71	25.4	3.2	3.8	12.04*
A19	99.80	2.79	2.69	42.7	2.9	4.3	13.29
A20	109.53	2.76	2.77	56.6	4.9	4.3	15.87
A21	151.59	2.79	2.70	51.9	3.9	4.0	9.16
A22	158.27	2.70	2.68	58.2	4.7	5.1	11.60
A23	171.86	2.79	2.67	38.0	14.7	4.2	11.95
A24	181.14	2.77	2.69	23.1	4.1	3.7	11.74
A25	201.19	2.80	2.67	49.8	10.4	3.2	10.57

* average effective porosity of reliable IMS specimens

Internal Distribution

1. L. D. Bates, 1001, MS-7169
2. F. P. Baxter, 3504, MS-6317
3. D. M. Borders, 1509, MS-6400
4. H. L. Boston, 4500-N, MS-6200
5. H. M. Braunstein, 130MIT, MS-6282
6. A. J. Caldanaro, 1509, MS-6400
7. R. B. Clapp, 1509, MS-6400
8. K. W. Cook, 1330, MS-7298
9. T. L. Cothron, 1001, MS-7155
19. J. H. Cushman, 1059, MS-6422
11. N. H. Cutshall, C207, MS-7172
12. M. F. P. DeLozier, 1037, MS-7355
13. A. F. Dieffendorf, 1509, MS-6400
14. W. E. Doll, 1509, MS-6400
15-21. J. Dorsch, 1509, MS-6400
22. R. B. Dreier, 1509, MS-6400
23. T. O. Early, 1509, MS-6400
24. J. M. Forstrom, 0303-8, MS-7314
25. D. E. Fowler, 1505, MS-6035
26. C. W. Francis, 3504, MS-6317
27. D. W. Frazier, 4500-N, MS-6198
28. B. J. Frederick, 4500-N, MS-6204
29. S. B. Garland, II, 7078-B, MS-6402
30. C. W. Gehrs, 1505, 6036
31. P. L. Goddard, 1330, MS-7298
32. J.-P. Gwo, 4500-N, MS-6203
33. C. S. Haase, 1330, MS-7298
34. R. D. Hatcher, Jr., 1509, MS-6400
35. D. S. Hicks, 1509, MS-6400
36. S. G. Hildebrand, 1505, MS-6037
37. J. Hodgins, 9983-58, MS-8248
38. Lucius Holder, Jr., 3001, MS-6029
39. D. D. Huff, 1509, MS-6400
40. G. K. Jacobs, 1505, MS-6036
41. W. K. Jago, 9207, MS-8225
42. P. M. Jardine, 1505, MS-6038
43. S. B. Jones, 9207, MS-8225
44. P. Kanciruk, 0907, MS-6490
45. R. H. Ketelle, 4500N, MS-6185
46. B. L. Kimmel, 4500-S, MS-6125
47. A. J. Kuhaida, 7078-B, MS-6402
48. R. R. Lee, 4500-N, MS-6185
49. S. Y. Lee, 1505, MS-6038
50. P. J. Lemiszki, 1509, MS-6400
51. R. S. Loffman, 4500-S, MS-6102
52. R. J. Luxmoore, 1505, MS-6038
53. J. F. McCarthy, 1505, MS-6036
54. L. W. McMahon, 9116, MS-8098
55. G. R. Moline, 1509, MS-6400
56. C. M. Morrissey, 1505, MS-6035
57. P. J. Mulholland, 1505, MS-6036
58. J. B. Murphy, 4500-N, MS-6198
59. C. E. Nix, 6026-C, MS-6395
60. M. J. Norris, 9983-AH, MS-8247
61. J. E. Nyquist, 1509, MS-6400
62. F. S. Patton, Jr., 1001-B, MS-7169
63. D. Pridmore, 6556F, MS-6348
64. T. Purucker, 105MIT, MS-6452
65. D. E. Reichle, 4500-N, MS-6253
66. C. T. Rightmire, 1509, MS-6400
67. T. H. Row, 4500-N, MS-6254
68. W. E. Sanford, 1509, MS-6400

69. F. E. Sharples, 1505, MS-6036
70. L. G. Shipe, 0303-8, MS-7314
71. D. S. Shriner, 1505, MS-6038
72. R. L. Siegrist, 1505, MS-6038
73. E. D. Smith, 1505, MS-6038
74. S. H. Stow, 1505, MS-6035
75. M. F. Tardiff, 4500-N, MS-6198
76. L. E. Toran, 1509, MS-6400
77. J. R. Trabalka, 3047, MS-6020
78. J. C. Wang, 4500-N, MS-6185
79. D. R. Watkins, 3504, MS-6317
80-84. D. B. Watson, 1509, MS-6400
85. O. R. West, 1505, MS-6036
86. R. K. White, 1330, MS-7298
87. S. L. Winters, 1509, MS-6400
88. T. F. Zondlo, 1509, MS-6400
89-93. ESD Library
94. Central Research Library
95. ORNL-Y-12 Technical Library
96-97. Laboratory Records Department
98. Laboratory Records, ORNL-RC
99. ORNL Patent Office

External Distribution

100. J. T. Ammons, Dept. of Plant and Soil Sci., University of Tennessee, TN 37901-1071
101. Jerry Archer, Geraghty & Miller Inc., 97 Midway Lane, Oak Ridge, TN 37830
102. Richard Arnseth, SAIC, 301 Laboratory Rd., Oak Ridge, TN 37830
103. Ernest Beauchamp, C-260 Jackson Plaza, MS-7614, R13, Oak Ridge, TN 37830
104. Robert Benfield, TDEC/DOE Oversight, 761 Emory Valley Rd., Oak Ridge, TN 37830
105. G. W. Bodenstein, USDOE-OR Federal Bldg., Oak Ridge, TN 37830
106. Paul Craig, Environmental Consulting Engineers, P.O. Box 22668, Knoxville, TN 37933
107. S. N. Davis, 6540 Box Canyon Drive, Tucson, AZ 85745
108. Director, Center for Management, Utilization, and Protection of Water Resources, Tennessee Technological University, P.O. Box 5082, Cookeville, TN 38505
109. S. G. Driese, Department of Geological Sciences, University of Tennessee, Knoxville, TN 37996
110. B. E. Dugan, Department of Civil and Mineral Engineering, University of Minnesota, Minneapolis, MN 55455
111. J. F. Franklin, College of Forest Resources, Anderson Hall AR-10, University of Washington, Seattle, WA 98185
112. P. M. Goldstrand, Department of Geological Sciences, MS-172, University of Nevada, Reno, NV 89557

113. Jim Harless, TDEC/DOE Oversight, 761 Emory Valley Rd., Oak Ridge, TN 37830

114. R. C. Harriss, Institute for the Study of Earth, Oceans, and Space, University of New Hampshire, Durham, NH 03824

115. P. Hofmann, Department of Energy, 3 Main St., Oak Ridge, TN 37830

116. G. M. Hornberger, Dept. of Environmental Sciences, University of Virginia, Charlottesville, VA 22903

117. G. Y. Jordy, Office of Program Analysis, Office of Energy Research, ER-30, G-226, USDOE, Washington, D.C. 20545

118-119. H. E. Julian, TVA Engineering Laboratory, PO Drawer E, Norris,TN 37828

120-124. T. J. Katsube, Geological Survey of Canada, Mineral Resources Division, 601 Booth Street, Ottawa, Ontario, CANADA K1A 0E8

125. D. C. Kopaska-Merkel, Geological Survey of Alabama, 420 Hackberry Lane, Tuscaloosa, AL 35486

126. O. C. Kopp, Department of Geological Sciences, University of Tennessee, Knoxville, TN 37996

127 P. E. Lamoreaux & Assoc. Inc., P.O. Box 2310, Tuscaloosa, AL 35403

128. D. A. Lietzke, Lietzke Soil Services, Route 3, Box 607, Rutledge, TN 37861

129. Changsheng Lu, Jacobs ER Team, 125 Broadway Ave. Oak Ridge, TN 37830

130. L. D. McKay, Department of Geological Sciences, University of Tennessee, Knoxville, TN 37996

131. W. M. McMaster, 1400 West Racoon Valley Rd.

132. Manager, CH2M Hill, 599 Oak Ridge Turnpike, Oak Ridge, TN 37830

133. Manager, HSW Environmental Consultants, 687 Emory Valley Rd., Oak Ridge, TN 37830

134. Manager, Radian/Lee Wan Assoc., 120 South Jefferson Circle, Oak Ridge, TN 37830

135. Manager, Systematic Management Services, 673 Emory Valley Rd., Oak Ridge, TN 37830

136. G. K. Moore, Route 4, Box 927, Waynesboro, TN 38485

137. Ronit Nativ, Dept. of Soil and Water Sci., Faculty of Agriculture, Hebrew University of Jerusalem, P.O. Box 12, Rehovot 76100, ISRAEL

138. M. J. Neton, Geologic & Environmental Services, 701 Cherokee Blvd., Suite G, Chattanooga, TN 37405

139. K. S. Novakowski, National Water Research Institute, 867 Lakeshore Rd., Burlington, Ontario L7R 4A6, CANADA

140. Chudi Nwangwa, TDEC/DOE Oversight, 761 Emory Valley Rd., Oak Ridge, TN 37830

141. R. H. Olsen, Microbiology & Immunology Dept., University of Michigan, Medical Sciences II, #5605, 1301 East Catherine St., Ann Arbor, MI 48109-0620

142. A. Patrinos, Environmental Sciences Division, Office of Health & Environmental Research, ER-74, USDOE, Washington, D.C. 20585

143. R. Pawlowicz, Bechtel, 151 Lafayette Dr. Oak Ridge, TN 37830

144. W. K. Puff, Dames and Moore, 575 Oak Ridge Turnpike, Oak Ridge, TN 37830

145. F. Quinones, Chief, Tennessee District, WRD, U.S. Geological Survey, 810 Broadway, Suite 500, Nashville, TN 37203

146. G. D. Reed, Dept. of Civil Engineering, University of Tennessee, 62 Perkins Hall, Knoxville, TN 37996-2010

147. N. Scromeda, Geological Survey of Canada, Mineral Resources Division, 601 Booth Street, Ottawa, Ontario, CANADA K1A 0E8

148. D. Shults, Tennessee Dept. of Environment and Conservation, Div. of Radiological Health, TERRA Bldg., 150 Ninth Ave. North, Nashville, TN 37243-1532

149. W. C. Sidle, Environmental Protection Division, USDOE-OR, P.O. Box 2001, Oak Ridge, TN 37831-8739

150. J. Smoot, Dept. of Civil Engineering, University of Tennessee, 62 Perkins Hall, Knoxville, TN 37996-2010

151. D. K. Solomon, 2381 Beacon Drive, Salt Lake City, Utah 84108

152. D. A. Stephenson, South Pass Resources, Inc., 8669 East San Alberto Drive, Suite 101, Scottsdale, AZ 85258

153. B. A. Tschantz, Dept. of Civil Engineering, University of Tennessee, 62 Perkins Hall, Knoxville, TN 37996-2010

154. G. van der Kamp, Environment Canada, 11 Innovation Blvd., Saskatoon, Saskatchewan S7N 3H5, CANADA

155. W. White, 542 Glenn Road, State College, PA 16803

156. F. J. Wobber, Environmental Sciences Division, Office of Health & Environmental Research, Office of Energy Research, ER-74, USDOE, Washington, D.C. 20585

157. J. Young, Camp Dresser & McGee, Suite 500, 800 Oak Ridge Turnpike, Oak Ridge, TN 37830

158-159. S. C. Young, Environmental Consulting Engineers, P. O. Box 22668, Knoxville, TN 37933

160. Office of Assistant Manager for Energy Research & Development, USDOE-OR, P.O. Box 2001, Oak Ridge, TN 37831-8600

161-163. Office of Scientific & Technical Information, P.O. Box 62, Oak Ridge, TN 37831